A new insight into catalytic ozonation of sulfasalazine antibiotic by plasma-treated limonite nanostructures: Experimental, modeling and mechanism

Zahra Heidari, Rasool Pelalak, Rahime Eshaghi Malekshah, Mahboubeh Pishnamazi, Mashallah Rezakazemi, Tejraj M. Aminabhavi, Saeed Shirazian

Publication date

01-01-2022

Published in

Licence

Document Version
1

Citation for this work (HarvardUL)

A new insight into catalytic ozonation of sulfasalazine antibiotic by plasma-treated limonite nanostructures: Experimental, modeling and mechanism

Zahra Heidari [a], Rasool Pelalak [b,c], Rahime Eshaghi Malekshah [d], Mahboubeh Pishnamazi [e], Mashallah Rezakazemi [f], Tejraj M. Aminabhavi [g,*], Saeed Shirazian [h,i,*]

[a] *Chemical Engineering Faculty, Sahand University of Technology, 51335-1996, Sahand New Town, Tabriz, Iran*
[b] *Institute of Research and Development, Duy Tan University, Da Nang 550000, Vietnam*
[c] *Faculty of Environmental and Chemical Engineering, Duy Tan University, Da Nang 550000, Vietnam*
[d] *Medical Biomaterial Research Centre (MBRC), Tehran University of Medical Sciences, Tehran, Iran*
[e] *Department of Chemical Sciences, Bernal Institute, University of Limerick, Limerick, Ireland*
[f] *Faculty of Chemical and Materials Engineering, Shahrood University of Technology, Shahrood, Iran*
[g] *School of Advanced Sciences, KLE Technological University, Hubballi, 580 031, India*
[h] *Faculty of Applied Sciences, Ton Duc Thang University, Ho Chi Minh City, Vietnam*
[i] *Bernal Institute, University of Limerick, Limerick, Ireland*

ARTICLE INFO

ABSTRACT

This study investigates the application of novel natural and plasma-treated iron (III) oxide-hydroxide (limonite) catalysts on the degradation/mineralization of sulfasalazine (SSZ) antibiotic by ozone-based advanced oxidation processes (AOPs). The limonite nanostructures were prepared by non-precursor, environmentally friendly, and fast glow discharge plasma technology under oxygen (PTL/O_2) and oxygen/argon (PTL/O_2/Ar) gaseous atmosphere. The characteristic analysis demonstrated enhanced surface area, morphology, active surface sites, and physical stability after the plasma treatment. It was found that SSZ degradation/mineralization was effectively improved (36%) in the heterogeneous catalytic ozonation process (HCOP) using PTL/O_2/Ar compared to sole ozonation. Modeling and optimization of SSZ degradation through the central composite design (CCD) and artificial neural network (ANN, topology of 4:7:1) showed that complete SSZ degradation can be achieved at the optimized condition (initial pH = 7, ozone concentration = 15 mg L^{-1}, catalyst loading = 1.5 g L^{-1} and treatment time = 50 min). The effect of organic and inorganic salts confirmed that the reactive oxygen species, mainly hydroxyl radicals, were responsible for SSZ degradation by HCOP. The main intermediates during SSZ oxidation were identified. The toxicity of SSZ solution and electrical energy consumption were decreased using PTL/O_2/Ar nanocatalysts in HCOP. Economic studies demonstrated 46% reduction in energy consumption of HCOP using PTL/O_2/Ar compared to NL samples. For the first time, molecular dynamics simulation was applied to provide a deeper insight into the adsorption mechanisms of SSZ and ozone onto limonite surface (1 1 1) during HCOP.

1. Introduction

Disposal of contaminated wastewaters produced by various human activities causes serious damage to aquatic wildlife, leading to a lack of access to clean water resources. The complex structures of released pollutants such as antibiotic pharmaceuticals make them resistant to classical treatment methods [1–4]. Therefore, effective treatment methods should be considered to remove hazardous pollutants from wastewaters. Sulfasalazine (SSZ) as a sub-group of sulfonamides antibiotics is mostly prescribed in treating intestinal inflammation, Crohn's disease, and rheumatoid arthritis [5,6]. The treatment of SSZ-containing wastewaters is impossible by bio-degradation alone, and disposal without an effective treatment would cause serious damage to aquatic ecosystem [5]. On the other hand, physical processes such as precipitation, adsorption, and membrane methods are not advantageous since they only can change the contaminants phase, thus they still required

more treatment [7–9].

As a practical removal approach, advanced oxidation processes (AOPs) can be employed successfully for the complete removal of a vast diversity of organic contaminants. In this method, a series of robust reactive oxygen species (ROSs), especially hydroxyl radicals ($^{\cdot}$OH), are produced from different sources during the process, which can remove the organic species with a stable chemical structure toward mineralization [10,11]. Applications of different AOPs, including photocatalysis [12,13], sonocatalysis [14], electro-Fenton [5,15], and ozone-based processes [16,17] have been reported for the elimination of organic pollutants from water and wastewater. The sole ozonation encountered some challenges such as inadequate solubility of O_3 molecules in water, production of disinfection and chemically resistant by-products during the reaction as well as the selective oxidation of organic pollutants by O_3 molecules [18]. Therefore, the application of ozone in conjunction with UV light [19] or H_2O_2 [20] and the introduction of catalysts [21,22] are common approaches. Application of solid particles as a catalyst in ozonation (heterogeneous catalytic ozonation, HCOP) can efficiently reduce the process costs compared to sole ozonation [23]. The presence of catalysts in the reaction medium enhance the rate and number of produced ROSs, which are necessary for the degradation reactants [6,23]. In this regard, Fe-containing natural minerals having low cost and eco-friendly nature have attained significant attention and have the possibility of separation from the reaction solution after the treatment [24]. Natural limonite (FeOOH, NL) catalysts can be considered as novel mineral oxyhydroxide catalyst in different AOPs because of rich active surface groups such as OH. It may be noted that mineral catalysts have some drawbacks such as transport resistance and restricted catalytic active sites. To overcome these limitations, nanosized catalysts appear to be a promising approach. The non-destructive, inexpensive, and free-precursor plasma technique can thus be useful for the production of nanostructures from the mineral catalysts to reduce their mass transfer problems. Moreover, this method by providing more accessible catalytic surface sites eventually generates more ROSs in the process [25]. Also, despite the mechanical processes such as high energy ball milling methods, plasma technique has higher efficiency, more control on the size/morphology of the produced samples with no risk of agglomeration and contamination of the samples [26].

The practical application of the selected treatment method requires detailed information about the interaction between the operating factors and their influence on each other. In addition, the optimization of treatment parameters is essential to achieve the highest contaminant degradation efficiency in AOPs. The classical one-factor-at-a-time method consumed a considerable time, which even cannot describe the interaction of the parameters. As an alternative approach, using modeling and optimization techniques such as central composite design (CCD) and artificial neural network (ANN) can effectively reduce the number of tests. The response surface methodology (RSM) through CCD performs based on the statistical technique as well as the ANN model uses the validation and training of the data [27].

The objectives of this study are: (1) investigate the degradation/ mineralization of 0.1 mM SSZ as a hazardous pharmaceutical contaminant through different AOPs such as O_3, O_3/H_2O_2 and HCOP using NL, PTL/O_2 and PTL/O_2/Ar nanocatalysts and comparison of the economic as well as electrical energy consumption of these processes, (2) for the first time, eco-friendly, available, and low-cost nanostructures of limonite with improved surface active sites were obtained via non-destructive, simple and quick cold plasma technologies using O_2 and O_2/Ar atmosphere and characterized by different analyses, (3) RSM and ANN modeling-based optimization techniques were used to model SSZ degradation by HCOP in order to evaluate the effect of main operating variables (initial pH, O_3 concentration, catalyst loading and treatment time), which are not reported yet, (4) the important role of ROSs and active sites in SSZ degradation mechanism have been evaluated in the presence of anionic salts (Cl$^-$, CO_3^{2-}, NO_3^- and $H_2PO_4^-$), BQ and TB, (5) the formation of aromatic intermediates and by-products during the SSZ

degradation by HCOP were evaluated by liquid chromatography-electrospray ionization-mass spectrometry (LC-ESI-MS) analysis, and (6) the molecular dynamics simulations were performed to get a deeper understanding of SSZ and O_3 adsorption mechanisms on the PTL/O_2/Ar nanocatalysts for the first time.

2. Materials and methods

2.1. Chemical reagents

The natural limonite was supplied from Kave Co. mineral (Yazd, Iran) and SSZ (>99%) was obtained from Sigma-Aldrich. All other used reagents were obtained from Merck Company (Germany) and were of analytical grade. Sodium thiosulfate (Na$_2$S$_2$O$_3$·5H$_2$O) was utilized to stop the degradation reactions at different times of reaction. Potassium hydrogen phthalate (C$_8$H$_5$KO$_4$, 99.5%) was used for calibration of total organic carbon (TOC).

2.2. Preparation of the limonite nanostructures

The natural limonite (NL) was crashed by ball-milling and then sieved and washed with deionized water to eliminate the impurities. The solution was then filtered and dried at 70 °C for 24 h before plasma treatment. The graphical steps for pretreatment of natural limonite samples are presented in Fig. S1. The specified amount of pretreated NL (3 g) was placed in the reactor of non-thermal glow discharge plasma. The plasma reactor includes a tubular shape Pyrex glass (5 cm diameter × 25 cm length) connected to a high voltage DC power supply. To provide the plasma environment (50 Pa-1150 V) the rotary-turbo-molecular pump and high voltage DC generator were utilized. The non-thermal glow discharge plasma through oxygen and mixed gases (argon and oxygen) atmosphere were applied to produce PTL/O_2 and PTL/O_2/Ar samples, respectively. The flows of O_2 and Ar gasses were adjusted at 3.5 cm^{3}s^{-1} to reach the required pressure. Under the mentioned conditions, O_2 gas was applied for 60 min to produce PTL/O_2 samples. Also, PTL/O_2/Ar samples were produced by applying O_2 gas for 15 min and 45 min of Ar gas. The obtained samples were used without any additional modifications. The schematic diagram of the plasma setup is presented in Fig. S2.

2.3. Limonite nanostructures characterizations

The chemical structure and crystalline phase of the natural and treated limonite catalysts were investigated by X-ray diffraction (XRD) using Siemens D5000 diffractometer (Germany). The surface morphology, size, and shape of the natural and treated catalysts were measured using the field emission scanning electron microscopy (FESEM; DSM-960A Zeiss, Germany) coupled with an EDX (energy dispersive X-Ray) analyzer. The available functional groups onto the surface of bare and modified samples were recognized by applying Fourier Transform Infrared Spectroscopy (FTIR, Bruker, Germany). The surface area, mean pore diameter, pore volume, and structure of the natural and treated catalysts were determined by the physical N_2 adsorption–desorption at 77.35 K using BELSORP-mini II (Japan) apparatus after degassing the samples at 383.15 K for 25 min. The elemental and chemical state of the samples was assessed by Thermo Fisher K-Alpha X-ray photoelectron spectroscopy (XPS) analysis. Concentration of the released Fe ions to the solution from limonite nanoparticles was determined by atomic absorption spectroscopy (AAS, Analytikjena, Germany). The point of zero charge (pH$_{PZC}$) of the natural and modified catalysts was evaluated using the salt addition method [12].

2.4. Modeling

2.4.1. CCD modeling

Table 1 shows the selected independent parameters (catalyst loading (g L^{-1}), treatment time (min), initial pH, and O_3 concentration (mg L^{-1})), and the levels of these parameters.

For statistical calculations, the g_i is defined in Eq. (1) [6]:

$$g_i = \frac{G_i - G}{\delta G} \tag{1}$$

where G_i refer to independent variables, G refer to real value of independent parameters and δ_G refers to the step change.

2.4.2. ANN modeling

The type of transfer function, the number of layers and nodes in a layer are important in describing the ANN (Artificial Neural Network) modeling's topology. The optimum ANN topology is usually determined by the trial-and-error method. In this modeling method, input variables are the same as those selected independent parameters for CCD modeling (Table 1). To determine the optimal data set the K-fold methodology was utilized (K = 3). Accordingly, 33% of empirical tests were used for the validation of the model. The *JMP Pro 14* software was employed for ANN modeling and analyzing the obtained results.

2.5. AOP experiments

The degradation of SSZ using HCOP was accomplished in a bubble column reactor in a semi-continuous mode. A cylindrical Pyrex reactor with a 35 cm height and an internal diameter of 4 cm was used to perform the degradation/mineralization (Fig. S3). An ozone generator was connected to a diffuser in the reactor to supply the required ozone (flow rate = 1 L.h^{-1}). In addition, a magnetic stirrer was used for better dispersion of the ozone in the SSZ aqueous solution. The ozone concentration was changed from 7 to 15 mg L^{-1} with an ozone analyzer. At specific reaction times, 4 mL of the solution was taken from the reactor and mixed with 1 mL of 0.01 M Na_2SO_3 to quench the degradation reactions. NaOH and/or H_2SO_4 solutions were used for pH adjustment and the solution pH was measured by pH-meter (Metrohm654, Switzerland). The amount of the residual O_3 molecules in the solution was measured using Indigo colorimetric method. The mineralization of SSZ was assessed by the TOC (VCSH-Shimadzu Corporation, Japan) analyzer. The effects of different organic and inorganic ions (benzoquinone (BQ), tertiary butyl alcohol (TBA), Cl$^-$, SO_4^{2-}, CO_3^{2-} and $H_2PO_4^-$) as the radical scavengers in different concentrations and the concentration of dissolved ozone was used to explore the mechanism of the reactions during degradation of SSZ by HCOP. The toxicity measurements of initial and treated solutions were evaluated by Microtox acute toxicity examination using the standard technique (ISO/DIS 11348–3) [28,29].

2.6. LC-ESI-MS analysis

The formed aromatic intermediates during HCOP were recognized using the LC-ESI-MS technology. The analyses were performed in a C18 column (100 mm × 2.1 mm, 100 Å) using an enhanced mass spectrum scan with a positive mode on an AB SCIEX 3200 QTRAP (Framingham, USA). The scanning conditions were as follows: mass scanning region

50–1000 *m/z*, sampling period: 0.1 s, CDL: 450 °C, and at the heating module temperature of 350 °C.

2.7. Toxicity measurements

The toxicity of control and treated solutions were evaluated by measuring bioluminescence inhibition of Vibrio Fischeri marine bacteria according to ISO 11348–3, 2007 instruction. The toxicity of 0.1 mM SSZ solution was determined by a Microtox Model 500 (M500) analyzer at 15 °C during 120 min of sole and catalytic ozonation. The toxicity results were expressed as the percent of the bioluminescence inhibition.

2.8. Computational methods

2.8.1. Simulation cell construction

Molecular dynamics (MD) simulations have been extensively used to study the reactivity of molecules and to explain the interactions of molecules with solid surfaces [30]. Here, the MD simulations were performed in *Materials Studio* software. The obtained unit cell model and snapshot of iron-oxyhydroxide surface (1 1 1) ($FeOOH_{(1\,1\,1)}$) structure are presented in Fig. S4(a)-(c). The simulation cell of iron-oxyhydroxide was made to a (1 1 1) surface. The supercell was formed with a thickness vacuum of 20.00 Å along with a slab position of 2.00. The outcomes of the optimized structures were obtained at $a = 31.08$ Å; $b = 16.44$ Å; $c = 26.21$ Å, $\alpha = \beta$; 90.00, and γ; 99.00 deg.

2.8.2. Computational details

Forcite module of *Material Studio* software was used for simulation of cell construction and molecular dynamic calculations. The periodically constrained $FeOOH_{(1\,1\,1)}$ was covered by SSZ and ozone molecules. Then, optimization of $FeOOH_{(1\,1\,1)}$-SSZ and $FeOOH_{(1\,1\,1)}$-ozone configurations were done using the *Forcite* module, and geometries were optimized using the cell parameters: $a = 31.08$ Å; $b = 16.44$ Å; $c = 26.21$ Å, $\alpha = \beta = 90.00$ and $\gamma = 99.00°$. The Dreiding force field was selected for molecular simulations of both $FeOOH_{(1\,1\,1)}$-SSZ and $FeOOH_{(1\,1\,1)}$-ozone configurations. Then molecular dynamic study (NVT, moles (N), volume (V), and temperature (T)) of $FeOOH_{(1\,1\,1)}$-SSZ and $FeOOH_{(1\,1\,1)}$-ozone was carried out by *Forcite* module using lattice parameters of $a = 31.08$ Å; $b = 16.44$ Å; $c = 26.21$ Å, $\alpha = \beta$; 90.00 °, and $\gamma = 99.00$ ° with a simulation time of 100 min.

3. Results and discussion

3.1. Limonite nanostructures characterizations

The shape and size of the limonite particles before and after plasma treatment were analyzed by FESEM technique and the outcomes are depicted in Fig. 1. As shown in Fig. 1(a-d), the natural limonite samples include the non-uniform bulky structures without specified orientations. On the other hand, by applying the plasma treatment, the morphology of NL was modified entirely, which is obvious in FESEM images (Fig. 1(e-l)). The enhanced morphological characteristics of samples after O_2 plasma modifications can be related to the cleaning effect of O_2 gas (Fig. 1(e-h)). The plasma treatment using O_2/Ar atmosphere results are shown in Fig. 1(i-l) where uniform nanorods were formed and a significant decrease in particle size was observed. The size of these particles was measured by Distance Measurement Software (Nahamin Pardazan Danesh Company), which showed that particle sizes were less than 20 nm (Fig. 1(l)). The produced similar size and shape of particles could be due to sputtering effect of Ar gas, which consequently improved specific surface area, but increment of the surface area can provide more accessibility to catalytic active sites.

XRD patterns of NL and limonite nanostructures produced by different atmospheric plasma treatment are depicted in Fig. 2(a). The diffraction peaks located at 2θ values of 17.78°, 21.25°, 26.35°, 33.22°, 34.70°, 47.26°, 50.65°, 53.22°, and 68.48° are related to characteristics

Table 1
The levels of the operating variables.

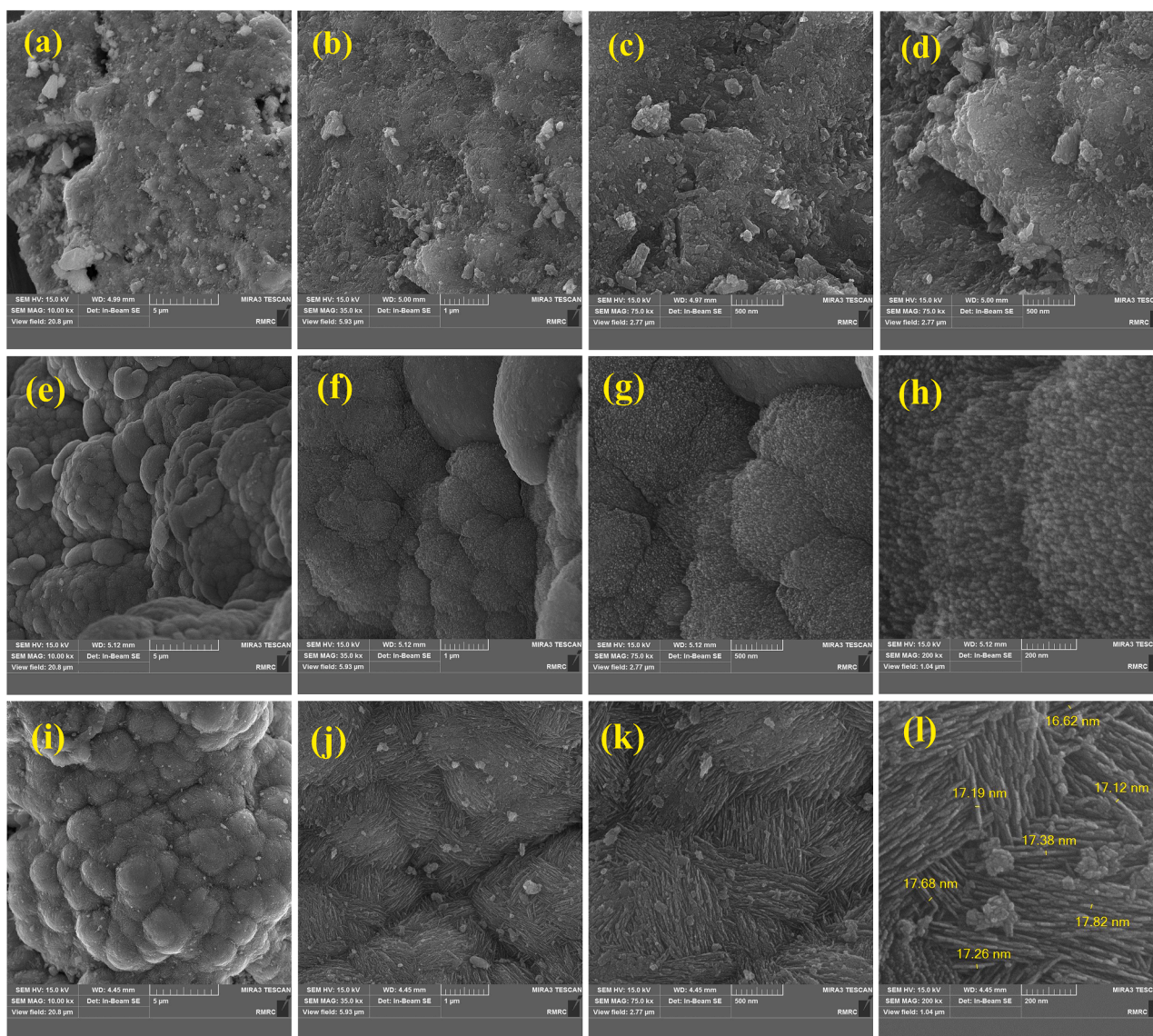| Variables	Ranges and levels				
	−2	−1	0	1	2
Initial ozone concentration (mg L^{-1}) (G_1)	7	9	11	13	15
Initial catalyst loading (g L^{-1}) (G_2)	0.5	0.75	1	1.25	1.5
Initial pH (G_3)	3	5	7	9	11
Time treatment (min) (G_4)	10	20	30	40	50

Fig. 1. The FESEM micrographs of the (a-d) NL samples, (e-h) plasma-treated limonite under O_2, and (i-l) O_2/Ar atmosphere samples.

of (0 2 0), (0 1 1), (0 2 1), (0 3 1), (1 2 0), (1 1 1), (1 1 2), (1 2 2) and (1 0 3) planes. The XRD patterns of natural and treated limonite samples showed insignificant changes in the position of XRD peaks, suggesting that the crystal structure of limonite remained unchanged after the plasma treatment. The average size of the nanostructure crystals calculated by the Debye–Scherrer equation [31,32] was 16.76 nm.

FTIR spectra of the unmodified and plasma-modified samples (with O_2 and O_2/Ar atmosphere) are shown in Fig. 2(b). In all the samples, the vibration mode of –OH bond related to surface absorbed water molecules and –OH group of limonite appeared at 3420 and 3133 cm^{-1}, respectively [33,34]. The peaks located at 1544 and 1640 cm^{-1} correspond to C–H bond vibration mode and peaks centered at 537 and 471 cm^{-1} can be linked to tensile vibrations mode of Fe-O bond [35,36]. Furthermore, the formation of surface Fe-OH groups has resulted in the appearance of absorption bands at 792, 901, and 1024 cm^{-1} [37]. A significant increase in the intensity of adsorption peaks, especially Fe-related peaks such as Fe-OH can be observed after the plasma treatment. This could be linked to removing impurities by the plasma irradiation and more accessibility of iron-rich surface sites of the limonite nanostructures [25,38], but no significant changes in the position of the peaks in the plasma-treated samples, indicating that the application of plasma technique has no negative effect on the chemical composition of

the resulting nanostructures.

The influence of plasma treatment on the surface properties of limonite, including surface area, pore structure, and pore volume was investigated using the nitrogen adsorption–desorption test, and the obtained results were analyzed using BET isotherm. Fig. 2(c) shows type-IV behavior (ISO 15901–2) for both the unmodified and plasma-modified samples according to IUPAC classification. A hysteresis loop (H4 type) can be observed in the samples' adsorption–desorption isotherms, revealing the porous structures of both the samples with a narrow gap *meso*-micro-pores. Also, the application of plasma treatment has transformed the close pores of NL samples into interconnected open pores. The surface area and total pore volume of natural limonite samples were obtained to be 32.51 m^2/g and 0.022 m^3/g, respectively, but these were increased to 43.25 m^2/g and 0.036 m^3/g after the O_2 plasma treatment. Moreover, the application of O_2/Ar as plasma atmosphere increased the surface area to 54.86 m^2/g and total pore volume to 0.042 m^3/g. The mean pores diameter of about 4.83, 4.56, and 3.15 nm was obtained for natural, O_2 and O_2/Ar treated samples, respectively.

XPS analysis was done to get better insights into the elemental and chemical compositions of natural and plasma-treated nanocatalysts. The wide-scan spectral results of XPS analysis for natural and treated samples are shown in Fig. 2(d). The results showed that the composition of
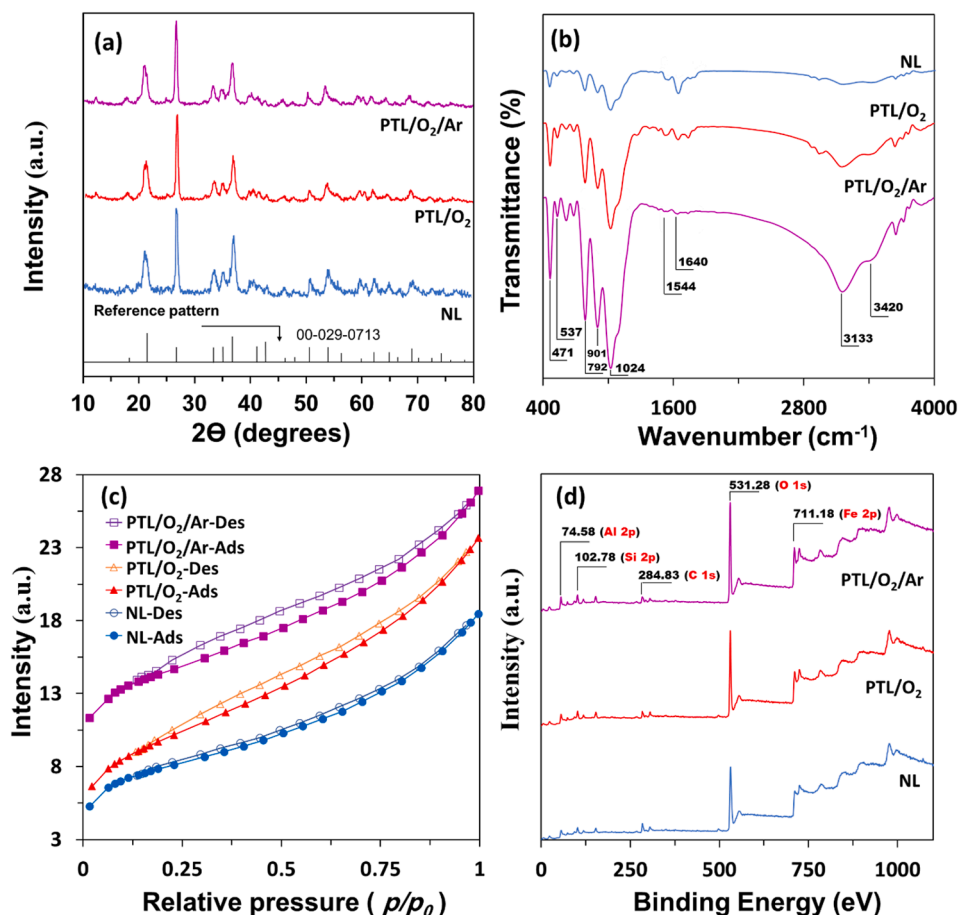
Fig. 2. (a) XRD patterns (b) FTIR spectra, (c) N_2 adsorption–desorption isotherms, (d) the XPS analysis for NL and PTL samples.

all the samples is formed from O and Fe as well as C, Al, and Si elements. As it is evident from Fig. 2(d), peaks at 711.18, 531.28, 284.83, 102.78, and 74.58 eV are attributed to the binding energy of Fe2p, O1s, C1s, Si2p, and Al2p transitions, respectively. Furthermore, deconvolution peaks of Fe2p, O1s, and C1s curves for XPS spectra of natural and plasma-treated catalysts are presented in Fig. 3. Fe2p XPS spectrum contained several wide peaks in the range 705–740 eV, which showed two dominant peaks. The peaks located at 710.17 and 724.35 eV are associated with $Fe2p_{3/2}$ and $Fe2p_{1/2}$, respectively, further demonstrating the Fe^{3+} in NL and plasma-treated samples [39]. The observed peak at 711.43 eV can be assigned to FeOOH in the limonite structure. Moreover, an enhancement in peak area was observed in the plasma-treated samples, which might provide more surface active sites for decomposition of ozone molecules [40], further improving the catalytic activity of plasma-treated samples. From Fig. 3, it can be observed that the deconvoluted spectrum of O1s peaks resulted in recognition of oxide and hydroxide groups at about 529.61, 531.28 eV, respectively as well as H_2O of limonite structure at 534.95 eV [41,42]. The peaks at 532.87 eV are attributed to O-Si. The XPS results in Fig. 3 imply the main C1s peaks located at 284.72 and 286.15 eV, which is related to C–C or C–H and C-O, respectively. Also, C1s peak corresponding to ester carbon atoms (O-C=O) at 288.26 eV, while the C1s peak assigned to C=O is observed at 289.59 eV [43]; notice that C1s peak area got reduced after the plasma treatment.

Furthermore, Al2p and Si2p peaks are depicted in Fig. S5 for the natural and plasma-treated samples. The Al2p peak related to Al-OH or Al_2O_3 is observed at 74.79 eV, while the main Si2p shows two peaks positioned at 99.52 and 103.21 eV, which are attributed to Si^0 and SiO_2, respectively. The net surface charge of the catalyst has an impact on the adsorption of pollutant or radical species in AOPs. For this purpose,

pH_{PZC} of NL and $PTL/O_2/Ar$ samples were measured using the salt addition technique. The plots of ΔpH (pH_f-pH_i) vs initial pH (pH_i) are shown in Fig. S6. Here, at pH values of 6.6 and 7.1, the value of ΔpH is zero for natural and modified structures, respectively, which can be related to pH_{PZC} of these samples; hence, by increasing the pH to more than these values surface of the particles acquired negative charge (anionic state of limonite), but lower pH values led to the positively charged surface due to the cationic state of limonite.

3.2. CCD modeling

The CCD model proposed 31 tests for four factors with five levels for SSZ degradation by HCOP in the presence of $PTL/O_2/Ar$ samples. Table 2 shows the list of runs, the model predicted values, and experimental values and Eq. (2) was used to obtain the predicted values using CCD model:

$$Y = F_0 + \sum_{i=1}^{k} F_i g_i + \sum_{i=1}^{k} F_{ii} g_i^2 + \sum_{i=1}^{k-1} \sum_{j=2}^{k} F_{ij} g_i g_j + \varepsilon \quad i \neq j \quad (2)$$

In this quadratic polynomial equation, Y is the predicted response by the model (SSZ degradation efficiency); F_0 is model constant, F_i, F_{ii} and F_{ij} are coefficients of model related to linear, quadratic, and interaction effect, respectively; g_i and g_j define the coded values variables from Eq. (2) and ε is the error. The index numbers of patterns are represented as i and j, while the number of variables is represented by k [38]. The relationship between independent parameters and removal efficiency of SSZ as the response of CCD model was established as per Eq. (3):
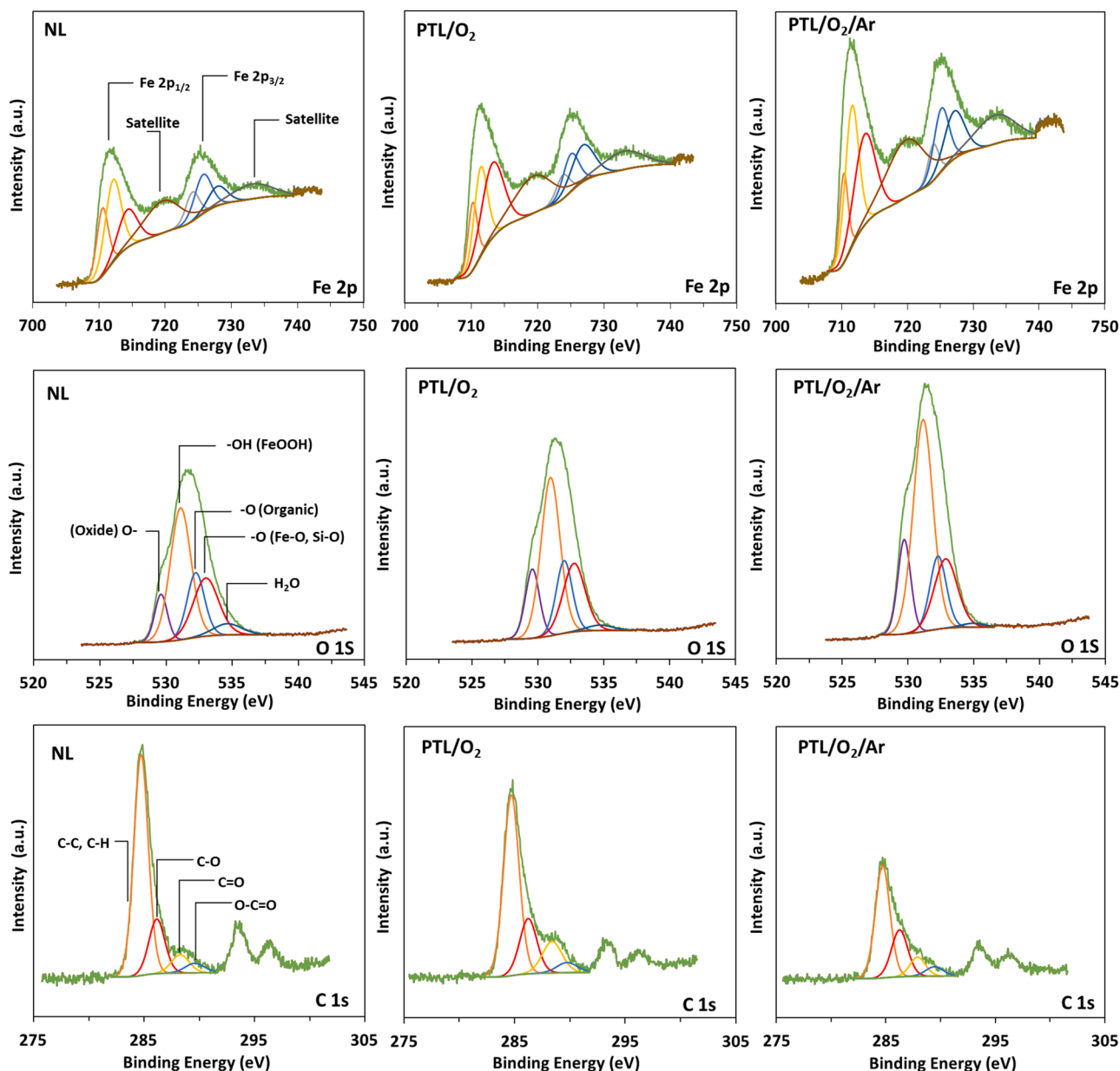
Fig. 3. Fe2p, O1s, and C1s curves of natural limonite, O_2, and O_2/Ar plasma treated limonite.

$$Y(Degradation\ Efficiency\ (DE\%)) = 66.07 + 6.62g_1 + 8.32g_2 + 1.36g_3$$
$$+ 6.80g_4 + 0.09g_1^2 - 0.35g_2^2 - 7.89g_3^2$$
$$+ 0.49g_4^2 - 0.97g_1g_2 - 0.67g_1g_3$$
$$- 0.02g_1g_4 + 0.86g_2g_3 - 0.92g_2g_4$$
$$- 0.35g_3g_4$$

$$(3)$$

The above Eq. (3) indicates that all the variables had a positive influence on SSZ degradation by the HCOP.

The evaluation of the importance and adequacy of the CCD model was carried out using the analysis of variance (ANOVA). As presented in Table 3, R^2 coefficient was 99.25%, which explains 99.25% of the variations in SSZ degradation by HCOP. Besides, the F-value of 150.68 being higher than the critical F-value, confirms the significant power of the CCD model for predicting SSZ degradation efficiency. The low P-values (less than 0.05) of linear and square parameters indicate a significant effect of these parameters on the response of the model.

In order to evaluate the adequacy of the obtained model, an appropriate tool is the analysis of residuals, which is the difference between the observed and the computed data. Fig. S7 shows the residual analysis for SSZ degradation by the HCOP process using limonite nanostructures. The formation of a straight line in the normal probability plot and random distribution of the points confirms the reasonability of the model.

The regression analysis for the empirical data, including estimated coefficients by the regression model, t and P-values are presented in Table S1. Evaluating the P-values confirmed that all the independent parameters, as well as interaction effects of the initial ozone concentration with treatment time, showed an important impact on the degradation efficiency of SSZ. Fig. S8 shows the effect of variables by the percentage values obtained from Eq. (4), which is named Pareto analysis. As can be observed, the dosage of catalyst, the initial pH of the solution, treatment time, and initial concentration of the ozone affect the SSZ degradation by 30.52, 27.43, 20.39, and 19.31%, respectively.

$$P_i = \left(\frac{F_i^2}{\sum F_i^2} \right) \times 100 \qquad i \neq 0 \qquad (4)$$

Table 2

The coded and uncoded matrix of CCD and ANN models, the predicted and experimental values for SSZ degradtion by HCOP using PTL/O$_2$/Ar nanocatalysts.

Run #	Coded variables				Uncoded variables				Removal efficiency (%)		
					C$_{O_3}$(mg/L)	C$_{cat}$ (g/L)	pH	Time (min)	Experimental	Predicted	
										CCD	ANN
1	−1	1	1	−1	9	1.25	9	20	58.11	58.41	55.41
2	0	0	−2	0	11	1	3	30	31.92	31.77	40.53
3	1	1	1	1	13	1.25	9	40	79.13	79.45	80.24
4	−1	1	−1	−1	9	1.25	5	20	52.20	51.93	46.69
5	0	0	0	0	11	1	7	30	66.73	66.07	65.14
6	0	0	0	2	11	1	7	50	82.70	81.65	80.07
7	1	1	−1	−1	13	1.25	5	20	64.20	64.63	64.06
8	1	−1	−1	1	13	0.75	5	40	66.50	65.89	65.18
9	0	0	0	0	11	1	7	30	66.10	66.07	65.14
10	0	0	0	0	11	1	7	30	63.20	66.07	65.14
11	1	−1	−1	−1	13	0.75	5	20	50.20	49.79	49.44
12	−1	1	1	1	9	1.25	9	40	68.80	69.53	68.91
13	1	1	−1	1	13	1.25	5	40	75.00	77.05	79.85
14	1	1	1	−1	13	1.25	9	20	68.30	68.42	67.22
15	0	0	0	0	11	1	7	30	64.50	66.07	65.14
16	1	−1	1	−1	13	0.75	9	20	50.00	50.14	48.67
17	−1	−1	1	1	9	0.75	9	40	51.80	51.07	50.19
18	−1	−1	−1	1	9	0.75	5	40	49.20	49.40	48.36
19	0	0	0	−2	11	1	7	10	53.40	54.43	49.91
20	0	0	0	0	11	1	7	30	67.23	66.07	65.14
21	0	0	2	0	11	1	11	30	37.10	37.23	51.22
22	−1	−1	−1	−1	9	0.75	5	20	33.85	33.22	32.89
23	0	2	0	0	11	1.5	7	30	82.90	81.29	82.09
24	−1	−1	1	−1	9	0.75	9	20	38.00	36.27	36.27
25	−2	0	0	0	7	1	7	30	51.90	53.20	50.34
26	2	0	0	0	15	1	7	30	81.00	79.69	79.24
27	−1	1	−1	1	9	1.25	5	40	64.88	64.43	62.60
28	1	−1	1	1	13	0.75	9	40	64.26	64.86	62.47
29	0	0	0	0	11	1	7	30	65.50	66.07	65.14
30	0	0	0	0	11	1	7	30	69.23	66.07	65.14
31	0	−2	0	0	11	0.5	7	30	46.40	47.99	46.34

Table 3

ANOVA for the evaluation of the importance of the regression model.

Source of variations	DF	Adjusted mean square	F-value	P-value
Regression model	14	412.52	150.68	0
Linear	4	968.03	353.59	0
Square	4	463.43	169.28	0
Interaction	6	6.94	3.01	0.036
error	16	2.74	–	–
Lack-of-fit	10	2.10	0.55	0.805
Pure error	6	3.80	–	–
$R^2 = 99.25$, $R^2_{adj} = 98.5$				

3.3. Modeling of SSZ degradation process by the ANN method

The input variables and selected responses for the ANN model are the same as the CCD model. The designed matrix by the CCD model (Table 2) was used for training and validation in the ANN model. To obtain optimized topology for the ANN model, different numbers in the range of 3–20 were examined for the number of neurons in the hidden layer. Finally, four input variables, seven neurons in one hidden layer, and a response (SSZ degradation) as output were obtained for the ANN model (topology of 4:7:1). Figure S9 shows the diagram of the obtained optimized model, and Table S2 summarizes the weight and the values of biases between ANN layers. The obtained R^2 value of 0.93 for the best trained ANN model showed an acceptable agreement between the predicted and empirical values.

3.4. ANN and CCD models comparison

The efficiency of two models for the prediction of SSZ degradation by HCOP was compared, and the results are presented in Fig. S10. According to Eqs. (5)-(7), the values of R^2 (coefficient of determination),

RMSE (root-mean-square error), and MAE (mean absolute error) were used to compare the accuracy of the models:

$$R^2 = \frac{\sum_{i=1}^{n}(\overline{y}_i - y_i)^2 - \sum_{i=1}^{n}(f_i - y_i)^2}{\sum_{i=1}^{n}(\overline{y}_i - y_i)^2} \tag{5}$$

$$RMSE = \left[\frac{\sum_{i=1}^{n}(f_i - y_i)^2}{n}\right]^{1/2} \tag{6}$$

$$MAE = \left(\frac{1}{n}\right)\sum_{i=1}^{n}|f_i - y_i| \tag{7}$$

As can be seen in Table 4, values of the RMSE and MAE for the ANN model were found to be 2.35 and 3.64, respectively and these values were 1.19 and 0.99 for the CCD model. The estimated R^2 values for CCD and ANN models were 0.991 and 0.930, respectively, implying the accuracy of the two models to predict the effectiveness of the input variables on SSZ degradation efficiency by HCOP. The reported data in Table 4 indicate that the CCD model predicts SSZ degradation with higher accuracy compared to ANN model.

3.5. The optimum condition for SSZ degradation by HCOP

Optimum values of the efficient variables were determined to obtain the highest SSZ degradation efficiency by the HCOP and response

Table 4

A comparison of CCD and ANN models for SSZ degradation by HCOP.

Parameters	CCD	ANN
Regression coefficient (R^2)	0.991	0.930
Root mean square error (RMSE)	1.188	3.641
Mean absolute error (MAE)	0.989	2.347

optimizer was implemented to obtain optimum values of the operating parameters, and these results are presented in Table 5. To confirm the obtained optimum parameters, confirmatory experiment were performed at these values. As per the degradation tests, almost complete degradation (98.8%) of 0.1 mM SSZ was achieved under the optimum conditions. As can be seen from Table 5, the experimental results were very close to the predicted values from CCD and ANN, which demonstrated the significance of the modeling approach and the adequate accuracy of the models. A detailed comparison of different AOPs in SSZ degradation and mineralization is presented in Table 6.

3.6. Impact of operating variables on SSZ degradation by HCOP using PTL/O₂/Ar
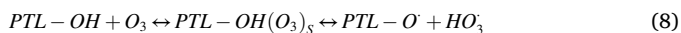
3.6.1. Impact of initial ozone concentration

The response surface and contour plots obtained from CCD (Fig. 4) and ANN (Fig. 5) models were utilized to describe the effect of O_3 initial concentration on the SSZ degradation. As can be observed in Fig. 4(a) and 5(a), increasing the concentration of the inlet ozone and also treatment time has led to the improvement in SSZ degradation. In AOPs, reactive radicals especially ˙OH are responsible for the degradation of the pollutants. With an increase in inlet ozone, the concentration of dissolved ozone and consequently ROSs production was enhanced. By increasing the ROSs generation, the SSZ degradation efficiency was also improved. Fig. 4(b) and 5(b) show the effect of pH variation with inlet ozone concentration on the degradation efficiency of SSZ. The experiments were accomplished at a constant catalyst dosage of 1 g L^{-1} and a reaction time of 30 min. As can be observed, the highest removal of SSZ was possible at pH of 7, which was near to the pH_{PZC} of the catalyst (7.1), but the removal efficiency declined at lower/higher pH values even with increasing the inlet ozone. The repulsion effect between the negatively charged catalyst surface and anionic form of SSZ molecules led to a reduction of process efficiency and the reason for this observation at pH lower than 7 may be related to the declined decomposition of O_3 molecules in acidic media. The effect of pH will be discussed in section 3.6.3 in more detail.

The changes in SSZ degradation efficiency with increasing catalyst loading and inlet ozone are depicted in Fig. 4(c) and 5(c), which shows that a higher amount of catalyst nanoparticles improved the SSZ degradation. Such a trend is possible because a higher amount of nanocatalysts and ozone concentration might have produced more ROSs in the solution, resulting in higher decomposition of the pollutants.

3.6.2. Effect of dosage of catalyst

Generally, catalyst dosage has a significant role in HCOP reactions that can affect the reaction rate and contaminant removal. Figures S11 (a) and (b) show the SSZ degradation efficiency vs catalyst loading in the range of 0.5–1.5 g/L, keeping the ozone concentration and pH constant (11 mg/L and 7, respectively).

Here, an increasing trend is observed for the SSZ degradation efficiency by increasing the catalyst loading. This can be explained due to the more number of available active sites of PTL/O₂/Ar nanocatalyst with increasing catalyst, which has resulted in a higher ozone decomposition and production of more ROSs spatially ˙OH to participate in SSZ degradation process as can be presented in Eqs. (8) and (11):
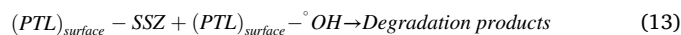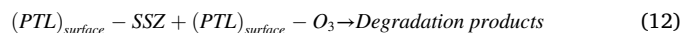
$$PTL - OH + O_3 \leftrightarrow PTL - OH(O_3)_S \leftrightarrow PTL - O^. + HO_3^. \qquad (8)$$

$$PTL - O^. + H_2O \leftrightarrow PTL - OH + {}^.OH \qquad (9)$$

$$HO_3^. \leftrightarrow H^+ + {}^.O_3^- \qquad (10)$$

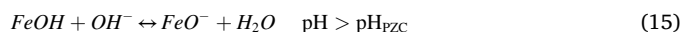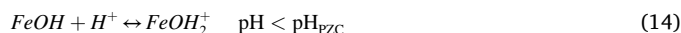$$HO_3^. \leftrightarrow {}^.OH + O_2 \qquad (11)$$

Another reason for the enhancement of catalytic efficiency with increasing nanocatalyst amount can be attributed for providing greater available PTL/O₂/Ar surface for the physical ozone and SSZ adsorption; their reaction on the catalyst surface can be given in Eqs. (12) – (13).

$$(PTL)_{surface} - SSZ + (PTL)_{surface} - O_3 \rightarrow Degradation\ products \qquad (12)$$

$$(PTL)_{surface} - SSZ + (PTL)_{surface} -{}^\circ OH \rightarrow Degradation\ products \qquad (13)$$

Therefore, by increasing the nanocatalyst concentration in the reaction medium at a constant contaminant concentration, the more available active surface area are present to produce additional ROSs as well as to adsorb SSZ or O_3 molecules.

3.6.3. Effect of solution pH

The role of initial pH on the degradation of SSZ by the catalytic ozonation under different pH conditions was examined and the results are depicted in Fig. S12. The initial O_3 concentration and catalyst loading were kept constant at 11 mg/L and 1 g/L, respectively. As can be seen from Fig. S12 the highest SSZ degradation was achieved at pH 7 and by increasing or decreasing the pH value, degradation of SSZ was decreased. In the catalytic ozonation processes, due to the synergistic effect of the catalyst and ozone, pH of the solution not only affected the ozone decomposition, but also influenced the surface charge properties of the catalyst (pH_{PZC}) as well as the adsorption behavior between the catalyst and the SSZ molecule. At different pH values of the solution, three types of functional groups ($FeOH_2^+$, FeOH, and FeO^-) could appear on the surface of PTL/O₂/Ar nanocatalysts as explained in Eqs (14) and (15):

$$FeOH + H^+ \leftrightarrow FeOH_2^+ \quad pH < pH_{PZC} \qquad (14)$$

$$FeOH + OH^- \leftrightarrow FeO^- + H_2O \quad pH > pH_{PZC} \qquad (15)$$

Based on the pH_{PZC} analysis when the pH is around 7, the predominant functional group in the catalyst surface is hydroxyl group (–OH), which can accelerate the decomposition of ozone and the production of ROSs. Another reason for higher removal efficiency of SSZ in natural pH is the dissociation of $HO_2^.$ to $O_2^{.-}$, which can participate in the SSZ decomposition. Similar results were reported in the literature [50]. The decline in the degradation of SSZ at higher pH values (pH of 9 and 11) could be related to the repulsion effect between the negative charges of SSZ ($pK_{a1} = 2.4$, $pK_{a2} = 8.3$ and $pK_{a3} = 11$) and the anionic surface of limonite structures. In pH values higher than pH_{PZC}, the SSZ structure acts as an anionic molecule and the surface charge of the plasma-treated catalysts becomes negative (FeO^-). Therefore, charge repulsion forces might have been created and as a result, the degree of SSZ adsorption and degradation can be reduced in basic pH. On the other hand, at lower pH values due to lower concentration of reactive species, the SSZ degradation efficiency also was decreased.

3.6.4. Comparison between CCD and ANN results

A comparative study was performed between the estimated values for SSZ degradation by CCD and ANN models and the experimental data. As can be observed in Fig. S13, the predicted results by ANN and CCD models are in good agreement with the experimental outcomes. The ability and reliability of both models were validated for predicting SSZ degradation by HCOP using PTL/O₂/Ar nanocatalysts.

3.7. Efficiency of different oxidation processes for the degradation of SSZ

The degradation of SSZ was investigated by various oxidation pro-

Table 5
Optimal values of the valiables for optimum 0.1 mM SSZ degradation.

O₃ (mg L⁻¹)	Cataylst (g L⁻¹)	pH	Time (min)	Degradation (%)		
				Predicted		Experimental
				CCD	ANN	
15.00	1.5	7	50.00	98.2	93.5	98.8

Table 6
Comparison of different AOPs for SSZ degradation/mineralization.

Method	catalyst	Experimental condition	Degradation	Mineralization	Ref.
Sonocatalysis	Nd-doped PbSe	[SSZ] = 0.025 mM [Cat] = 1 g L^{-1} pH = 4	80% (90 min)	–	[44]
Fenton-like	Fe^{3+}	[SSZ] = 0.25 mM [Fe^{3+}] = 0.20 mM [H_2O_2] = 12 mM pH = 3	Almost complete (60 min)	41% (60 min)	[5]
Heterogeneous electro-Fenton	$Fe@Fe_2O_3$	[SSZ] = 0.075 mM pH = 6	Almost complete (100 min)	Almost complete (360 min)	[45]
Photocatalytic degradation	$Na_4W_{10}O_{32}$	[SSZ] = 0.05 mM [H_2O_2] = 1 mM [Cat] = 0.04 mM pH = 4	25% (120 min)	Almost complete (48 h)	[46]
Photocatalytic degradation	NiO-ZnO	[SSZ] = 0.017 mM [Cat] = 0.7 g L^{-1} pH = 6.5	Almost complete (90 min)	Almost total COD removal (30 min)	[47]
Sonocatalysis	Pyrite nanoparticles	[SSZ] = 0.025 mM [Cat] = 0.5 g L^{-1} pH = 4	Almost complete (30 min)	–	[48]
Sonocatalysis	$Ag_2O/CdO/CeO_2/rGO$	[SSZ] = 0.025 mM [Cat] = 1.2 g L^{-1}	95% (20 min)		[49]
Catalytic ozonation	Limonite nanoparticles	[SSZ] = 0.1 mM [Cat] = 1.5 g L^{-1} [O_3] = 15 mg L^{-1} pH = 7	Almost complete (50 min)	78.5% (120 min)	This study

cesses including sole ozonation, ozonation/H_2O_2, adsorption, and catalytic ozonation using both natural and plasma-modified limonite. As can be observed in Fig. 6(a), the adsorption results of SSZ onto NL and PTL/O_2/Ar surface were 7.4 and 10.6%, respectively. Higher adsorption of SSZ by the PTL/O_2/Ar can be related to the enhanced surface area of the catalyst after plasma treatment. The equilibrium adsorption value of SSZ by PTL/O_2/Ar was calculated to be 0.164 mg/g PTL/O_2/Ar after 50 min of the adsorption process [51,52]. As can be observed, 62.8% of SSZ was removed by the direct and/or indirect attack of ozone molecules in the sole ozonation process. The introduction of NL and PTL/O_2/Ar could have enhanced the removal efficiency to 74.9 and 98.8%, respectively. The degradation of SSZ in the presence of limonite structures was accelerated due to hydroxyl groups and Fe ions of the catalyst [53]. The ozone reaction with surface hydroxyl groups of PTL/O_2/Ar nanostructures led to the production of ·OH and other ROSs, which has promoted SSZ decomposition. The proposed mechanism for SSZ degradation in the presence of limonite nanostructures in the catalytic ozonation process can be described by Eqs. (9)- (12). Furthermore, after the plasma treatment and by removing the impurities, more surface hydroxyl groups and Fe ions were accessible (Eqs. (16) and (17)):

$$Fe^{2+} + O_3 \rightarrow FeO^{2+} + O_2 \tag{16}$$

$$FeO^{2+} + H_2O \rightarrow Fe^{3+} + \cdot OH + {}^-OH \tag{17}$$

3.8. Electrical energy consumption and TOC removal

Fig. 6(b) shows the TOC removal and electrical energy consumption during SSZ decomposition by different degradation processes after 120 min of treatment. As can be seen, 78.5% of TOC was omitted during catalytic ozonation using PTL/O_2/Ar. The sole ozonation, ozone + H_2O_2, catalytic ozonation using NL structures could remove 42.5, 54.1, and 61.4% of TOC, while the application of plasma-treated limonite nanostructures significantly enhanced the SSZ mineralization. To select the most appropriate and cost-effective wastewater treatment process, several parameters need to be considered such as economics (operating, maintenance, and capital costs), and the quality of the effluent, but during the ozone-based AOPs electric energy consumption a large part of operating costs are included, where economic calculations were done by

assessing the electrical energy consumption, which in AOPs was evaluated as per Electrical Energy per Order (E_{EO}) concept provided by the International Union of Pure and Applied Chemistry (IUPAC); where E_{EO} is the required electrical energy (in kWh) to purify contaminated water (1 m^3) by 1 order of magnitude. The electrical energy consumption of different oxidation processes was calculated as:

$$E_{EO} = \frac{P \times t \times 1000}{V \times log\left(\frac{TOC_0}{TOC_f}\right)} \tag{18}$$

where P is input power (kW) of the system, t is processing time (h), V is volume (L) of reaction medium; TOC_0 and TOC_f are initial and final total organic carbons (mg/L), respectively. The calculated E_{EO} values for SSZ removal using various treatment techniques under optimum operating conditions are presented in Fig. 6(b). The calculated E_{EO} for ozonation with plasma-treated samples (175.5 kWh m^{-3}) was significantly lower compared to the sole ozonation (468.2 kWh m^{-3}), ozonation in the presence of H_2O_2 (325.1 kWh m^{-3}), and non-treated samples (271.1 kWh m^{-3}). The results confirmed the efficient application of plasma technique in the treatment of natural samples and hence, HCOP using PTL/O_2/Ar nanostructures can be considered as the most efficient process from the viewpoint of energy consumption. The price of electricity is 0.075 $ per kiloWatt-hour (kWh) in Iran, and hence the cost of electrical energy consumption for SSZ removal from 1 m^3 contaminated water by HCOP using natural and treated limonite will be 13.16 and 24.38 $, respectively. The application of plasma treatment has led to 46% reduction in the cost of electrical energy. In addition, the electrical energy cost of ozonation and ozone + H_2O_2 process were 35.11 and 20.33 $, respectively.

3.9. Reusability and stability of the prepared catalyst

One of the important factors in the long-time application of the catalysts is the stability of the catalyst in consequent applications. In this regard, the reusability of natural and plasma-modified limonite in catalytic ozonation was investigated in five repetitive cycles. After each run, the used catalyst particles were collected from the reaction media and rinsed several times with water, dried, and then utilized for the next run. XRD patterns of fresh and used PTL/O_2/Ar nanocatalysts in five

Fig. 4. 2D and 3D plots of the SSZ degradation efficiency: effect of O$_3$ concentration (mg/L) versus: (a) reaction time (min), (b) initial pH, and (c) PTL/O$_2$/Ar loading (g/L) estimated by CCD method.

runs shown in Fig. 6(c) show a negligible difference between the two patterns, demonstrating high stability of the synthesized samples. The reusability results given in Fig. 6(d) revealed a slight decrease in the efficiency of the catalyst and the efficiency of the catalyst decreased from 98.8 to 91.4% after five cycles. The nanocatalyst poisoning by the pollutants or intermediates could be the probable reason for such a slight loss of the nanocatalyst activity over five repeated runs. Furthermore, the concentration of Fe ions release in the reaction medium for both NL and PTL/O$_2$/Ar during the HCOP process was determined by AAS. Fig. 7 (a) shows the content of Fe ions in the reaction medium after treatment with NL and PTL/O$_2$/Ar were obtained as 0.221 and 0.062 mg/L,

respectively, indicating a decline in the Fe release from the catalyst structure and improvement in catalyst stability after the plasma treatment. This can be due to the solidifying and consolidation of the ions inside the PTL/O$_2$/Ar molecular structure after the plasma treatment. These data are in consistent with those reported by Rahemi et al. [54], in which, the authors showed the effect of non-thermal plasma treatment on the improvement of Ni/Al$_2$O$_3$–ZrO$_2$ nanocatalysts stability. Similarly, Khataee et al. [55] investigated the effect of Ar glow discharge plasma treatment on pyrite nanostructure stability, where about 13% reduction in catalyst reusability was observed after five consecutive cycles in the degradation of textile dye.
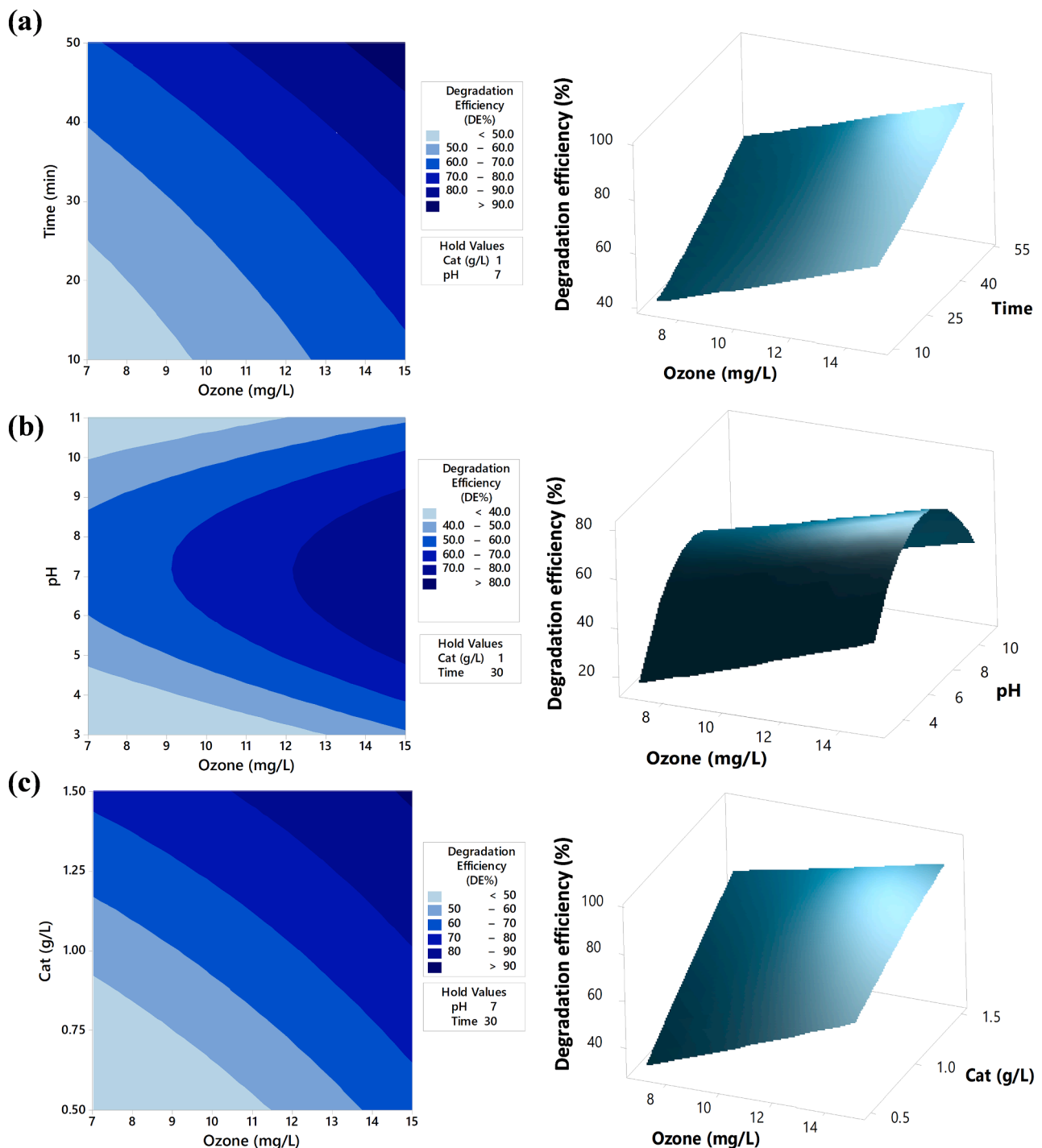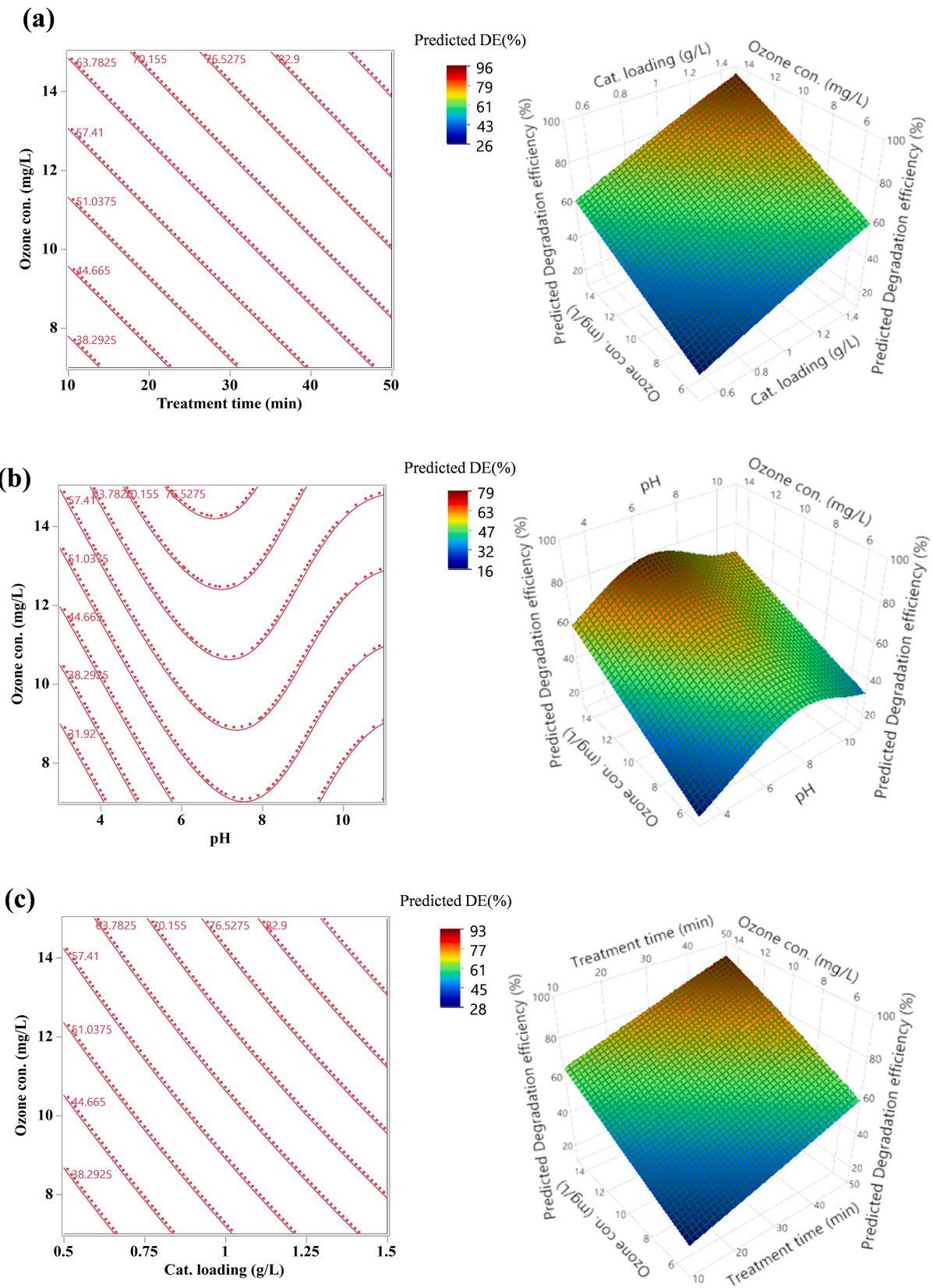
(a)

(b)

(c)

Fig. 5. 2D and 3D plots of the SSZ degradation efficiency: effect of O_3 concentration (mg/L) versus: (a) reaction time (min), (b) initial pH, and (c) PTL/O_2/Ar loading (g/L) estimated by ANN method.
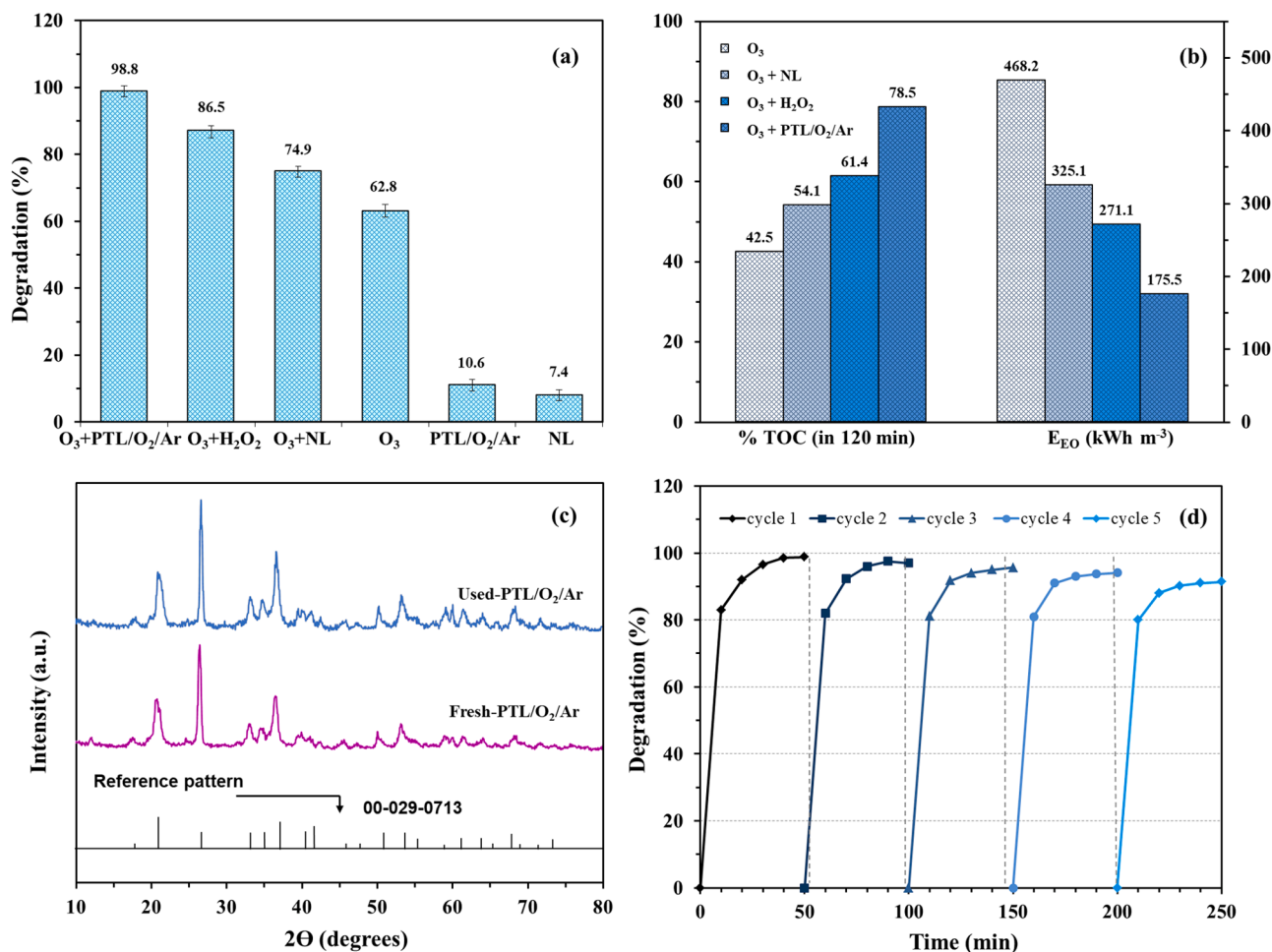
Fig. 6. Comparison of different oxidation methods for: (a) SSZ degradation efficiency and (b) TOC removal and electrical energy consumption, (c) the XRD patterns of fresh and used nanocatalysts and (d) SSZ degradation over 5 cycles in the HCOP process ($[SSZ]_0 = 0.1$ mM, $[O_3]_0 = 15$ mg/L, catalyst dosage = 1.5 g/L, pH = 7).

3.10. Effect of radical scavengers and anionic species

To confirm the role of free radicals and reactive oxygen species in SSZ decomposition by catalytic ozonation, the presence of different concentrations of radical scavengers (TBA and BQ) in the reaction solution were investigated and results are reported in Fig. 7(b). TBA and BQ react as a scavenger with hydroxyl and superoxide radicals, respectively. As seen from Fig. 7(b), the reaction in the absence of scavengers exhibits a complete decomposition of SSZ. The addition of 1 mM of TBA to reaction solution declined the degradation efficiency to 52.8 and 73.2% for ozonation alone and in the presence of PTL/O$_2$/Ar nanocatalysts, respectively, indicating the production of ·OH from ozone decomposition during the reaction [56]. Furthermore, the higher efficiency of HCOP confirmed the effective role of limonite nanostructure in ·OH generation. Fig. 7(c) represents 28.7 and 7.9% reduction in SSZ degradation efficiency in the presence of BQ in HCOP using PTL/O$_2$/Ar and the sole ozonation process, respectively confirming the importance of superoxide radicals in SSZ degradation, while inhibiting the effect of the radical scavengers indicate that free radicals viz. ·OH, O$_2^{\cdot-}$ were responsible for improving the degradation efficiency.

To evaluate the effect of surface hydroxyl groups of limonite and to simulate the real wastewater matrix, the influence of anionic ions (Cl$^-$, CO$_3^{2-}$, NO$_3^-$ and H$_2$PO$_4^-$) in the solution was studied. As can be seen in Fig. 7(d) the presence of anionic species declined the SSZ decomposition and the observed reduction was due to adsorption of anions onto the surface of limonite samples occupied with active sites of the catalyst [44,57]. Furthermore, the added anions reacted with the produced

hydroxyl radicals to decrease the concentration of ROSs as per the following reactions [14,58,59]:

$$CO_3^{2-} + \cdot OH \rightarrow CO_3^{\cdot-} + OH^- \tag{19}$$

$$NO_3^- + \cdot OH \rightarrow NO_3^\cdot + OH^- \tag{20}$$

$$H_2PO_4^- + \cdot OH \rightarrow H_2PO_4^\cdot + OH^- \tag{21}$$

$$Cl^- + \cdot OH \rightarrow \cdot ClOH^- \tag{22}$$

3.11. Analysis of SSZ degradation intermediates and by-products

Identification of the intermediates during SSZ degradation by HCOP in the presence of PTL/O$_2$/Ar was evaluated by LC-MS and the detected aromatic intermediates, as well as the by-products, are depicted in Fig. 8. The attack of hydroxyl radicals on the SSZ molecule ($m/z = 399$) has led to the production of intermediates with $m/z = 283$ (as the result of N = N bond cleavage) and $m/z = 338$ (as the result of N-C bond cleavage).

More hydroxylation of the first structure can produce C$_5$H$_6$N$_2$SO$_4$ with $m/z = 191$. The latter structure ($m/z = 338$) may further oxidize through desulfonation reaction giving $m/z = 275$, which then dehydroxylated to an intermediate with m/z of 243. Another possible pathway is azo bond cleavage of the intermediate with $m/z = 338$, which might have produced the structure with $m/z = 205$. Higher oxidation of intermediates might have led to denitrogenation to give $m/z = 95$. The generated intermediates undergo multiple reactions with
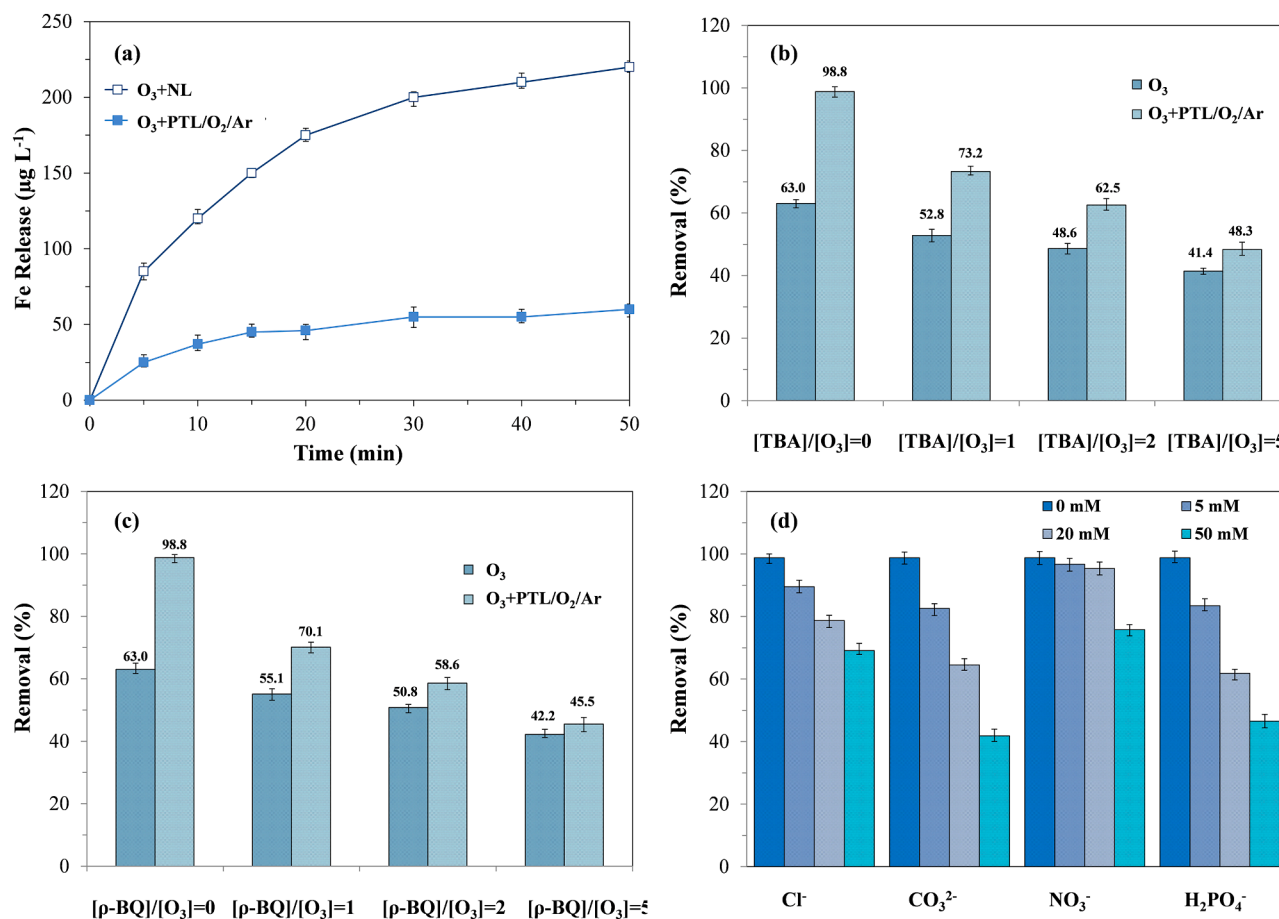
Fig. 7. (a) Fe ion release during various processes, (b) effect of TBA, (c) BQ and (d) different inions on SSZ degradation by ozonation and HCOP ([SSZ]$_0$ = 0.1 mM, [O$_3$]$_0$ = 15 mg/L, catalyst dosage = 1.5 g/L, pH = 7).

ROSs and bond cleavage might have occurred, leading to the generation of end-products namely, water, CO$_2$, and N ions.

3.12. Toxicity evaluation

In wastewater treatment processes, it is very important to study the toxicity of the system because toxicity of the obtained solution may be higher than the initial solution. Therefore, the toxicity of SSZ solution was evaluated during the treatment by the sole ozonation process and HCOP in the presence of PTL/O$_2$/Ar. The SSZ solution of 0.1 mM was treated at 120 min by both the processes, and the obtained results are illustrated in Fig. S14. As can be seen toxicity of the medium as a function of treatment time increased during the early stages of the re-action to about 90% in both processes. This can be due to the production of intermediates such as aromatic components, which are more toxic compared to the initial SSZ solution. Finally, 15.5% of inhibition remained in the solution treated by the sole ozonation process, while ozonation by PTL/O$_2$/Ar reduced the toxicity to 6%. The higher toxicity of the final solution in the ozonation process is because of the lower mineralization ability of this process compared to HCOP, which is in agreement with the obtained results in section 3.8. These results confirmed that the HCOP by PTL/O$_2$/Ar can efficiently detoxify SSZ solutions.

3.13. Mechanisms of heterogeneous catalytic ozonation process in presence of FeOOH catalysts

3.13.1. Plausible reaction mechanisms

The mechanism of HCOP can occur in both liquid and solid phases.

Although many parameters affect the reaction mechanism, and it is difficult to find an individual mechanism, there could be three possible general mechanisms, which are presented in Fig. 9 and these include: (a) adsorption of both pollutant and ozone molecules onto the surface of the catalyst and reaction on the solid phase (Fig. 9(a)), (b) adsorption of ozone molecules onto the surface of the catalyst, decomposition of ozone molecules to ˙OH and oxidation reaction takes place in the liquid bulk through the attack of ˙OH to the pollutant molecules (Fig. 9(b)), (c) adsorption of pollutant molecules onto the catalyst surface and reaction with ozone molecules and/or the produced ˙OH in the bulk of the liquid (Fig. 9(c)).

3.13.2. Molecular dynamic calculations

To investigate the mechanism of SSZ degradation by catalytic ozonation in the presence of PTL/O$_3$/Ar, the molecular dynamic approach was applied. Hence, the optimized structures of SSZ and ozone molecules were calculated using *Materials Studio* software which is displayed in Fig. S15. Moreover, the geometry optimization of FeOOH$_{(111)}$-SSZ and FeOOH$_{(111)}$-ozone structures were performed using the *Forcite* module and the results are presented in Figs S16 and S17. The initial energy value of FeOOH$_{(111)}$-SSZ configuration (828.29 kcal/mol) was shifted to lower energy value of 46.41 kcal/mol after optimization (Fig. S16(a)- (d)), while the initial energy value of FeOOH$_{(111)}$-ozone configuration (4708.91 kcal/mol) was shifted to a much lower energy value of −2.33 kcal/mol (Fig. S17(a)- (d)). Oxygen atoms of ozone in FeOOH$_{(111)}$-ozone system interacted with Fe(III) of FeOOH$_{(111)}$ surface by forming non-bonded interaction (-2.337 kcal/mol) including the van der Waals interaction (-2.28 kcal/mol) and long-range correction (-0.05 kcal/mol). E$_{int}$, the average interaction energy in the solid-state was
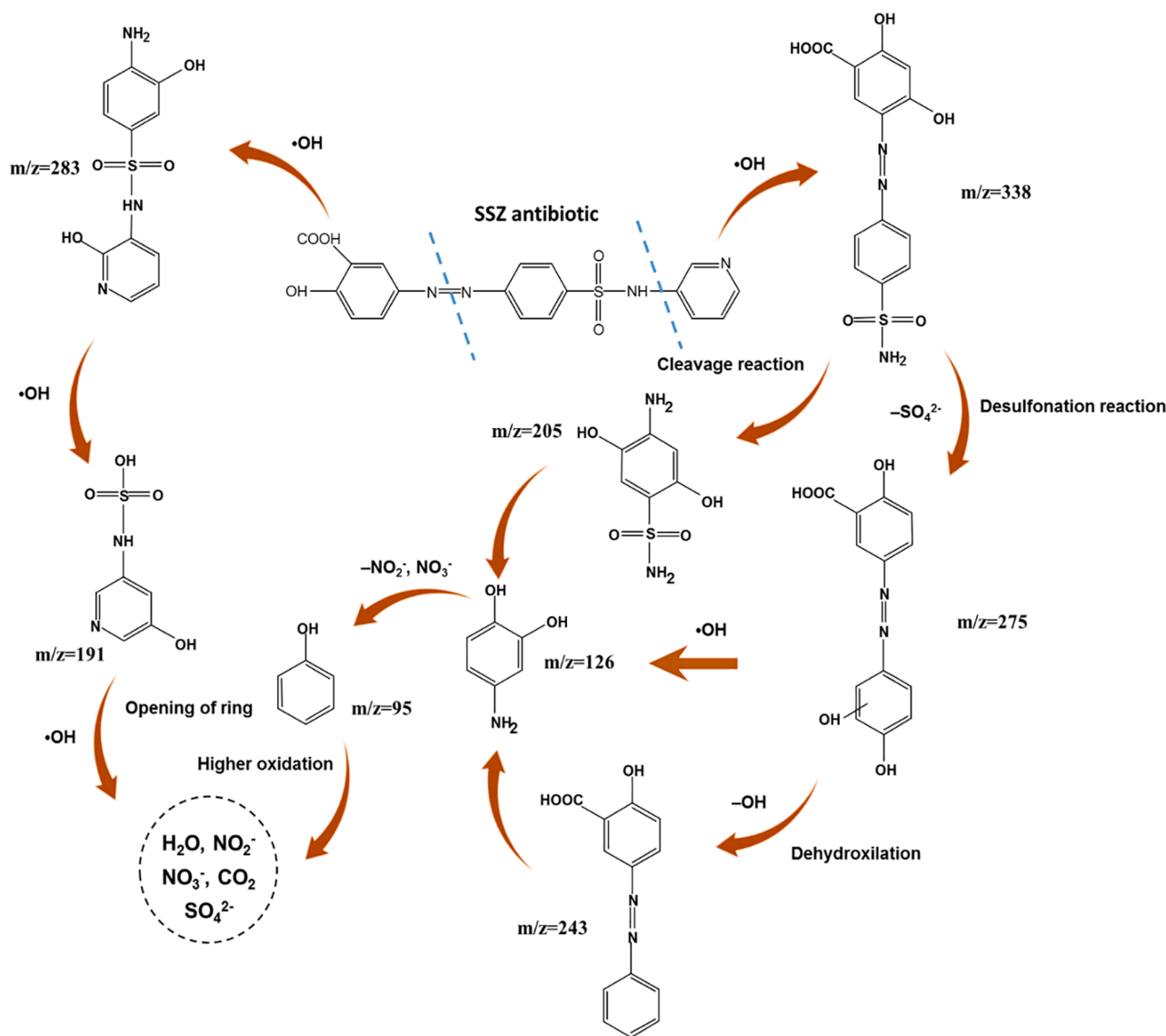
Fig. 8. Proposed SSZ degradation pathways in HCOP using PTL/O$_2$/Ar nanocatalysts.

calculated using [60,61]:

$$E_{int} = E_{total} - (E_{FeOOH} + E_{Ozone/SSZ}) \qquad (23)$$

where E$_{total}$ is total optimized energy of the binary system (FeOOH$_{(111)}$ surface-SSZ or FeOOH$_{(111)}$ surface-ozone), E$_{FeOOH}$ is the total optimized energy of FeOOH surface and E$_{ozone/SSZ}$ is the total optimized energy of the ozone or SSZ molecules in the system. Based on the molecular dynamic calculations total energy (E$_{total}$) of FeOOH$_{(111)}$ surface-SSZ and FeOOH$_{(111)}$ surface-ozone were 46.41 and −2.33 kcal/mol, respectively. The energy of FeOOH configuration (E$_{FeOOH}$) for both the systems was 4852 kcal/mol. In addition, energies of ozone (E$_{ozone}$) and SSZ (E$_{SSZ}$) system were −0.011 and 4.86 kcal/mol, respectively. The sum of adsorption energies of the components in FeOOH$_{(111)}$ surface-SSZ and FeOOH$_{(111)}$ surface-ozone systems were −4810.45 and −4854.33 kcal/mol, respectively. According to the calculations, more negative interaction energy was obtained for adsorption of ozone molecules on FeOOH$_{(111)}$ surface compared to SSZ molecules, indicating a considerable adsorption ability of ozone onto FeOOH$_{(111)}$ and higher binding affinity than the SSZ [62].

3.13.3. Molecular dynamic calculations (NVT ensemble) for FeOOH$_{(111)}$-SSZ and FeOOH$_{(111)}$-ozone structures

The adsorption dynamic simulations of both SSZ and ozone molecules onto FeOOH$_{(111)}$ surface were conducted under the canonical ensemble (NVT; moles (N), volume (V), and temperature (T)) to ensure the equilibrium system. After the geometry optimization, NVT calculations were performed for FeOOH$_{(111)}$-SSZ and FeOOH$_{(111)}$-ozone configurations at 298.0 K and 1 atm to obtain the possible states of these structures in the system. The final dynamic energy value of 47.175 kcal/mol was obtained for FeOOH$_{(111)}$-SSZ configuration, which was much lower than its initial energy value (113.723 kcal/mol) .As shown in Fig. 10(a), the hydrogen atom of benzene ring in SSZ molecule interacted with Fe(III) of FeOOH$_{(111)}$ surface by forming non-bonded interactions (-1.822 kcal/mol) including the van der Waals interactions (-1.822 kcal/mol) with H-Fe length of 2.191 Å. SSZ molecule interacts with the oxygen of FeOOH$_{(111)}$ surface via the formation of bonds between carbon (2.836 Å), hydrogen (2.254 Å) and azo (2.604 and 2.431 Å) atoms. In addition, aromatic rings of SSZ were placed in parallel above the FeOOH$_{(111)}$ surface due to azo and amine groups. The ellipsoidal snapshots of SSZ onto the FeOOH$_{(111)}$ surface are shown in Fig. S18(a) and (b).

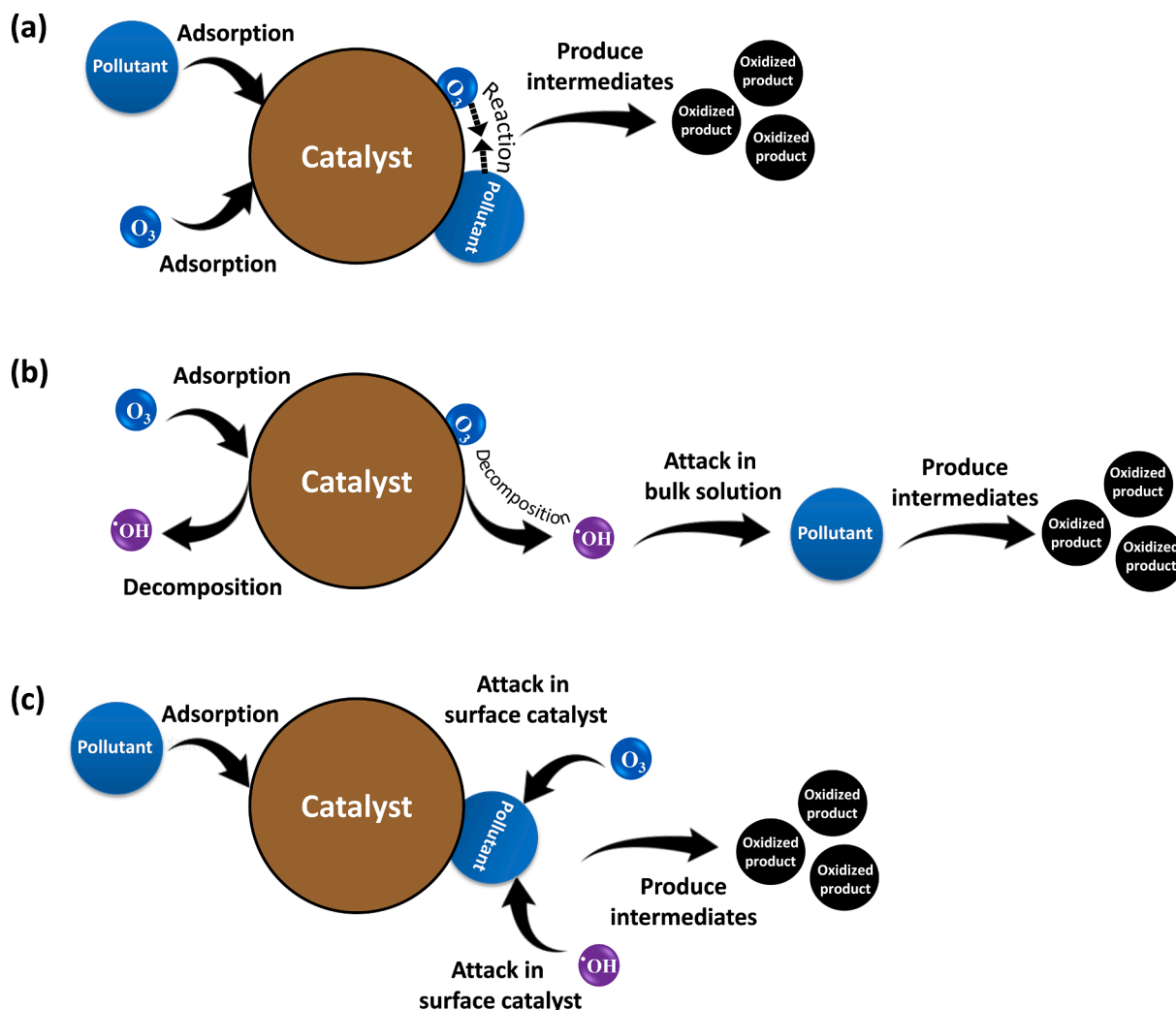Similarly, NVT calculations of ozone molecule onto FeOOH(111)

Fig. 9. Three possible cases of heterogeneous catalysis ozonation processes.

surface showed the final dynamic energy value of −0.522 kcal/mol by forming non-bonded interactions including the van der Waals interactions, which was much lower than its initial energy (0.320 kcal/mol) (Fig. 10(b)). The ellipsoidal snapshots of ozone onto FeOOH$_{(1 1 1)}$ surface are presented in Fig. S19(a) and (b). From the obtained results, it can be said that interaction of ozone molecules with FeOOH$_{(1 1 1)}$ surface (-0.522 kcal/mol) was more favorable than the SSZ molecule (47.175 kcal/mol). The interaction between ozone molecule and FeOOH surface is in good accordance with other experimental observations [63,64].

The distance of ozone molecule thermodynamically could be dominant on the FeOOH$_{(1 1 1)}$ surface with a length of 3.55 Å using the NVT calculations. The total energy of ozone molecules on iron-oxyhydroxide surface system under NVT condition showed high energy interactions compared to SSZ on iron-oxyhydroxide surface (1 1 1) [65].

4. Conclusions

In this research, degradation/mineralization of SSZ antibiotic (0.1 mM) as an emerging contaminant was investigated by the ozone-based advanced processes using natural and plasma-treated limonite. The novel limonite nanostructures with improved surface properties were synthesized from the available low-cost natural limonite by green, free-precursor, and cold glow discharge plasma method under different atmospheres. FESEM analysis confirmed the production of nanosized structures with uniform size and morphology owing to the cleaning and

sputtering effect of O$_2$ and Ar gases. The performance of NL and PTL/O$_2$/Ar samples in HCOP showed 74.9 and 98.8% of degradation and 54.1 and 78.5% of SSZ mineralization, respectively, while 62.8 and 42.5% were achieved in the sole ozonation process.

The impact of operating parameters on SSZ degradation was investigated and optimized using CCD and ANN models. A good agreement was found between the predicted values of the two models and the empirical results (R^2 = 0.991, MAE = 0.989, RMSE = 1.188 for CCD model, and R^2 = 0.930, MAE = 2.347, RMSE = 3.641 for ANN model). The presence of scavengers and anionic salts indicated that free radicals are the dominant species in the SSZ degradation process. Higher reduction in electrical energy consumption (62.5%) and toxicity were observed in O$_3$ + PTL/O$_2$/Ar process compared to O$_3$ process. Based on these detected species of LC-ESI-MS analysis, two main reaction routes were proposed for the degradation of SSZ by the ˙OH oxidation.

The reaction mechanism studies using the molecular dynamic simulations showed the adsorption and interaction of SSZ and ozone molecules onto FeOOH$_{(1 1 1)}$ surface in HCOP via the non-bonded spatially van der Waals interactions. Overall, the results indicated that utilization of available mineral catalysts as well as physical modification techniques can be promising to improve the ozonation process for the decontamination of wastewaters in terms of degradation efficiency and cost-effectiveness.
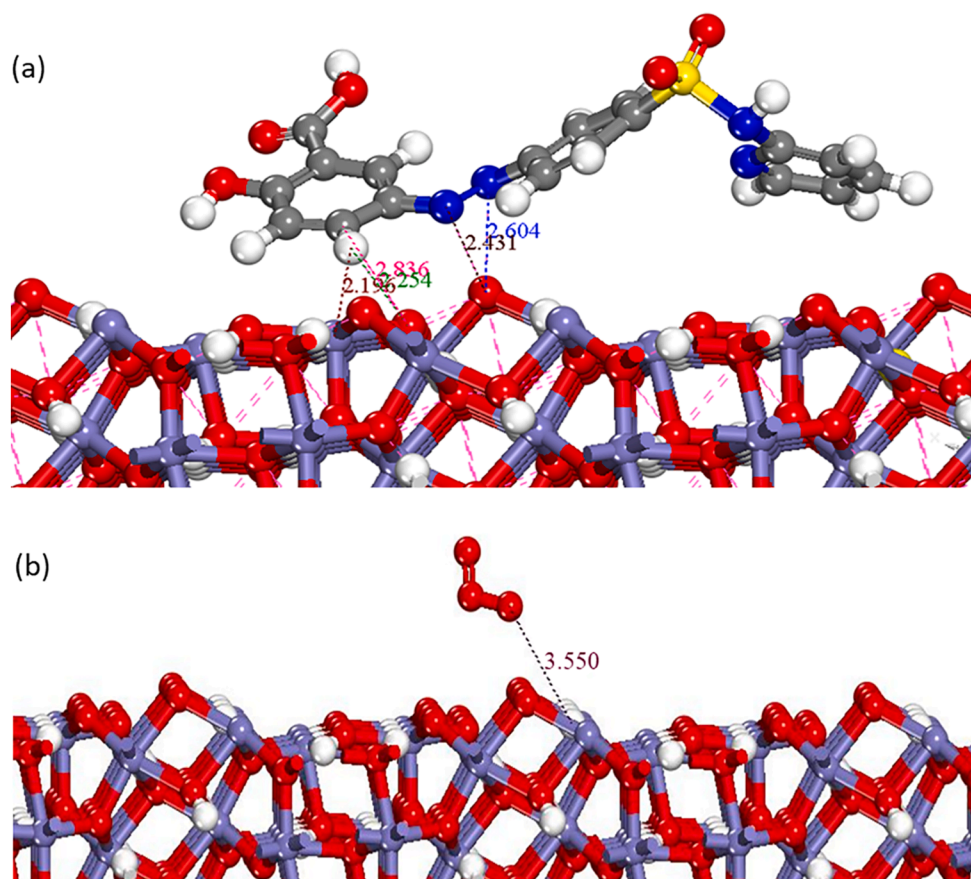
Fig. 10. Equilibrium configurations of adsorption of (a) SSZ and (b) ozone molecules onto iron-oxyhydroxide surface (1 1 1) from NVT molecular dynamics. Blue is N, light grey is H, dark grey is C, red is O, and yellow is S in SSZ molecule. Blue is Fe, light grey is H, and red is O on the iron-oxyhydroxide surface.

Declaration of Competing Interest

The authors declare that they have no known competing financial interests or personal relationships that could have appeared to influence the work reported in this paper.

Appendix A. Supplementary data

Supplementary data to this article can be found online at https://doi.org/10.1016/j.cej.2021.131230.

References

[1] F.J. Beltrán, A. Aguinaco, J.F. García-Araya, Mechanism and kinetics of sulfamethoxazole photocatalytic ozonation in water, Water Res. 43 (2009) 1359–1369.
[2] F.J. Beltrán, A. Aguinaco, J.F. García-Araya, Kinetic modelling of TOC removal in the photocatalytic ozonation of diclofenac aqueous solutions, Appl. Catal. B 100 (2010) 289–298.
[3] Y. Zhang, J. Zhou, J. Chen, X. Feng, W. Cai, Rapid degradation of tetracycline hydrochloride by heterogeneous photocatalysis coupling persulfate oxidation with MIL-53 (Fe) under visible light irradiation, J. Hazard. Mater. 392 (2020), 122315.
[4] R. Pelalak, Z. Heidari, M. Forouzesh, E. Ghareshabani, R. Alizadeh, A. Marjani, S. Shirazian, High performance ozone based advanced oxidation processes catalyzed with novel argon plasma treated iron oxyhydroxide hydrate for phenazopyridine degradation, Sci. Rep. 11 (2021) 964.
[5] X. Fan, H. Hao, X. Shen, F. Chen, J. Zhang, Removal and degradation pathway study of sulfasalazine with Fenton-like reaction, J. Hazard. Mater. 190 (2011) 493–500.
[6] R. Pelalak, R. Alizadeh, E. Ghareshabani, Z. Heidari, Degradation of sulfonamide antibiotics using ozone-based advanced oxidation process: Experimental, modeling, transformation mechanism and DFT study, Sci. Total Environ. 734 (2020), 139446.
[7] M. Kamali, D. Suhas, M.E. Costa, I. Capela, T.M. Aminabhavi, Sustainability considerations in membrane-based technologies for industrial effluents treatment, Chem. Eng. J. 368 (2019) 474–494.
[8] T. Tavangar, M. Karimi, M. Rezakazemi, K.R. Reddy, T.M. Aminabhavi, Textile waste, dyes/inorganic salts separation of cerium oxide-loaded loose nanofiltration polyethersulfone membranes, Chem. Eng. J. 385 (2020), 123787.
[9] R. Pelalak, Z. Heidari, S.M. Khatami, T.A. Kurniawan, A. Marjani, S. Shirazian, Oak wood ash/GO/Fe3O4 adsorption efficiencies for cadmium and lead removal from aqueous solution: kinetics, equilibrium and thermodynamic evaluation, Arabian J. Chem. 14 (2021), 102991.
[10] M. Karaca, M. Kıranşan, S. Karaca, A. Khataee, A. Karimi, Sonocatalytic removal of naproxen by synthesized zinc oxide nanoparticles on montmorillonite, Ultrason. Sonochem. 31 (2016) 250–256.
[11] M.A. Oturan, J.-J. Aaron, Advanced oxidation processes in water/wastewater treatment: principles and applications a review, Crit. Rev. Environ. Sci. Technol. 44 (2014) 2577–2641.
[12] Z. Heidari, R. Alizadeh, A. Ebadi, N. Oturan, M.A. Oturan, Efficient photocatalytic degradation of furosemide by a novel sonoprecipited ZnO over ion exchanged clinoptilolite nanorods, Sep. Purif. Technol. 242 (2020), 116800.
[13] A. Khataee, A. Karimi, R.D.C. Soltani, M. Safarpour, Y. Hanifehpour, S.W. Joo, Europium-doped ZnO as a visible light responsive nanocatalyst: Sonochemical synthesis, characterization and response surface modeling of photocatalytic process, Appl. Catal. A 488 (2014) 160–170.
[14] A. Khataee, A. Karimi, A. Hasanzadeh, S.W. Joo, Kinetic modeling of sonocatalytic performance of Gd-doped CdSe nanoparticles for degradation of Acid Blue 5, Ultrason. Sonochem. 39 (2017) 344–353.
[15] Z. Heidari, R. Pelalak, R. Alizadeh, N. Oturan, S. Shirazian, M.A. Oturan, Application of mineral iron-based natural catalysts in electro-fenton process: a comparative study, Catalysts 11 (2021).
[16] R. Pelalak, Z. Heidari, R. Alizadeh, E. Ghareshabani, N. Nasseh, A. Marjani, A. B. Albadarin, S. Shirazian, Efficient oxidation/mineralization of pharmaceutical

pollutants using a novel Iron (III) oxyhydroxide nanostructure prepared via plasma technology: experimental, modeling and DFT studies, J. Hazard. Mater. 411 (2021) 125074, https://doi.org/10.1016/j.jhazmat.2021.125074.

[17] A. Aghaeinejad-Meybodi, A. Ebadi, S. Shafiei, A. Khataee, M. Rostampour, Degradation of antidepressant drug fluoxetine in aqueous media by ozone/H2O2 system: process optimization using central composite design, Environ. Technol. 36 (2015) 1477–1488.

[18] A.N. Pisarenko, B.D. Stanford, D. Yan, D. Gerrity, S.A. Snyder, Effects of ozone and ozone/peroxide on trace organic contaminants and NDMA in drinking water and water reuse applications, Water Res. 46 (2012) 316–326.

[19] I. Bavasso, C. Poggi, E. Petrucci, Enhanced degradation of paracetamol by combining UV with electrogenerated hydrogen peroxide and ozone, J. Water Process Eng. 34 (2020), 101102.

[20] Z. Qiang, C. Liu, B. Dong, Y. Zhang, Degradation mechanism of alachlor during direct ozonation and O3/H2O2 advanced oxidation process, Chemosphere 78 (2010) 517–526.

[21] W. An, L. Tian, J. Hu, L. Liu, W. Cui, Y. Liang, Efficient degradation of organic pollutants by catalytic ozonation and photocatalysis synergy system using double-functional MgO/g-C3N4 catalyst, Appl. Surf. Sci. 534 (2020), 147518.

[22] Z. Yan, J. Zhu, X. Hua, D. Liang, D. Dong, Z. Guo, N. Zheng, L. Zhang, Catalytic ozonation for the degradation of polyvinyl alcohol in aqueous solution using catalyst based on copper and manganese, J. Cleaner Prod. 272 (2020), 122856.

[23] J. Wang, H. Chen, Catalytic ozonation for water and wastewater treatment: Recent advances and perspective, Sci. Total Environ. 704 (2020) 135249, https://doi.org/10.1016/j.scitotenv.2019.135249.

[24] H. Chen, J. Wang, MOF-derived Co3O4-C@ FeOOH as an efficient catalyst for catalytic ozonation of norfloxacin, J. Hazard. Mater. 403 (2020), 123697.

[25] A. Khataee, P. Gholami, B. Vahid, S.W. Joo, Heterogeneous sono-Fenton process using pyrite nanorods prepared by non-thermal plasma for degradation of an anthraquinone dye, Ultrason. Sonochem. 32 (2016) 357–370.

[26] X. Yu, W. Shou, B.K. Mahajan, X. Huang, H. Pan, X. Yu, W. Shou, B.K. Mahajan, P. H. Pan, Materials, processes, and facile manufacturing for bioresorbable electronics: a review, Adv. Mater. 30 (2018) 1707624.

[27] A. Aghaeinejad-Meybodi, A. Ebadi, S. Shafiei, A. Khataee, M. Rostampour, Modeling and optimization of antidepressant drug fluoxetine removal in aqueous media by ozone/H2O2 process: comparison of central composite design and artificial neural network approaches, J. Taiwan Inst. Chem. Eng. 48 (2015) 40–48.

[28] I. Sirés, E. Brillas, M.A. Oturan, M.A. Rodrigo, M. Panizza, Electrochemical advanced oxidation processes: today and tomorrow, A review, Environmental Science and Pollution Research 21 (2014) 8336–8367.

[29] G. Mosoarca, C. Vancea, S. Popa, S. Boran, C. Tanasie, A green approach for treatment of wastewater with manganese using wood ash, J. Chem. Technol. Biotechnol. 95 (2020) 1781–1789.

[30] R. Pelalak, R. Soltani, Z. Heidari, R.E. Malekshah, M. Aallaei, A. Marjani, M. Rezakazemi, T.A. Kurniawan, S. Shirazian, Molecular dynamics simulation of novel diamino-functionalized hollow mesosilica spheres for adsorption of dyes from synthetic wastewater, J. Mol. Liq. 322 (2020), 114812.

[31] R. Darvishi Cheshmeh Soltani, A.R. Khataee, M. Mashayekhi, Photocatalytic degradation of a textile dye in aqueous phase over ZnO nanoparticles embedded in biosilica nanobiostructure, Desalination and Water Treatment, 57 (2016) 13494-13504.

[32] A. Rezaee, H. Masoumbeigi, R.D.C. Soltani, A.R. Khataee, S. Hashemiyan, Photocatalytic decolorization of methylene blue using immobilized ZnO nanoparticles prepared by solution combustion method, Desalin. Water Treat. 44 (2012) 174–179.

[33] R. Pelalak, Z. Heidari, Lithographically cut multiwalled carbon nanotubes: opening caps, controlling length distribution, and functionalization, J. Dispersion Sci. Technol. 35 (2014) 808–814.

[34] Z. Heidari, R. Alizadeh, A. Ebadi, R. Pelalak, N. Oturan, M.A. Oturan, Degradation of furosemide using photocatalytic ozonation in the presence of ZnO/ICLT nanocomposite particles: experimental, modeling, optimization and mechanism evaluation, J. Mol. Liq. 319 (2020), 114193.

[35] I.R. Guimarães, A.S. Giroto, W.F. de Souza, M.C. Guerreiro, Highly reactive magnetite covered with islands of carbon: oxidation of N and S-containing compounds in a biphasic system, Appl. Catal. A 450 (2013) 106–113.

[36] S. Rakshit, D. Sarkar, E.J. Elzinga, P. Punamiya, R. Datta, Mechanisms of ciprofloxacin removal by nano-sized magnetite, J. Hazard. Mater. 246 (2013) 221–226.

[37] X. Yan, J. Shao, Q. Wen, J. Shen, Stabilization of soil arsenic by natural limonite after mechanical activation and the associated mechanisms, Sci. Total Environ. 708 (2020), 135118.

[38] R. Pelalak, R. Alizadeh, E. Ghareshabani, Enhanced heterogeneous catalytic ozonation of pharmaceutical pollutants using a novel nanostructure of iron-based mineral prepared via plasma technology: a comparative study, J. Hazard. Mater. 392 (2020) 122269, https://doi.org/10.1016/j.jhazmat.2020.122269.

[39] M. Sun, R. Senthil, J. Pan, S. Osman, A. Khan, A facile synthesis of visible-light driven rod-on-rod like α-FeOOH/α-AgVO3 nanocomposite as greatly enhanced photocatalyst for degradation of rhodamine B, Catalysts 8 (9) (2018) 392, https://doi.org/10.3390/catal8090392.

[40] J. Nawrocki, B. Kasprzyk-Hordern, The efficiency and mechanisms of catalytic ozonation, Appl. Catal. B 99 (2010) 27–42.

[41] S. Desireddy, S. P.C, S. M. Maliyekkal, Anoxic ammonia removal using granulated nanostructured Fe oxyhydroxides and the effect of pH, temperature and potential inhibitors on the process, Journal of Water Process Engineering, 33 (2020) 101066.

[42] A.P. Grosvenor, B.A. Kobe, N.S. McIntyre, Studies of the oxidation of iron by water vapour using X-ray photoelectron spectroscopy and QUASES™, Surf. Sci. 572 (2004) 217–227.

[43] Z.-D. Huang, B. Zhang, R. Liang, Q.-B. Zheng, S.W. Oh, X.-Y. Lin, N. Yousefi, J.-K. Kim, Effects of reduction process and carbon nanotube content on the supercapacitive performance of flexible graphene oxide papers, Carbon 50 (2012) 4239–4251.

[44] A. Khataee, S. Arefi-Oskoui, A. Karimi, M. Fathinia, Y. Hanifehpour, S.W. Joo, Sonocatalysis of a sulfa drug using neodymium-doped lead selenide nanoparticles, Ultrason. Sonochem. 27 (2015) 345–358.

[45] S. Amali, M. Zarei, M. Ebratkhahan, A. Khataee, Preparation of Fe@Fe2O3/3D graphene composite cathode for electrochemical removal of sulfasalazine, Chemosphere 273 (2020), 128581.

[46] P. Cheng, Y. Wang, M. Sarakha, G. Mailhot, Enhancement of the photocatalytic activity of decatungstate, W10O324−, for the oxidation of sulfasalazine/sulfapyridine in the presence of hydrogen peroxide, J. Photochem. Photobiol., A 404 (2021) 112890.

[47] M. Rezaei, A. Nezamzadeh-Ejhieha, The ZnO-NiO nano-composite: a brief characterization, kinetic and thermodynamic study and study the Arrhenius model on the sulfasalazine photodegradation, Int. J. Hydrogen Energy 45 (2020) 24749–24764.

[48] A. Khataee, S. Fathinia, M. Fathinia, Production of pyrite nanoparticles using high energy planetary ball milling for sonocatalytic degradation of sulfasalazine, Ultrason. Sonochem. 34 (2017) 904–915.

[49] H. Mirzazadeh, M. Lashanizadegan, Ag2O/CdO/CeO2/reduced graphene oxide: synthesis, characterization and its application as catalyst for sulfasalazine, diclofenac and phenol degradation under ultrasonic irradiation, Mater. Res. Express 6 (2019) 065008.

[50] M. Fathinia, A. Khataee, S. Aber, A. Naseri, Development of kinetic models for photocatalytic ozonation of phenazopyridine on TiO2 nanoparticles thin film in a mixed semi-batch photoreactor, Appl. Catal. B 184 (2016) 270–284.

[51] R.D.C. Soltani, A. Rezaee, G.S. Khorramabadi, K.J.W.s. Yaghmaeian, Optimization of lead (II) biosorption in an aqueous solution using chemically modified aerobic digested sludge, Water Science and Technology, 63 1 (2011) 129-135.

[52] R.D.C. Soltani, A.J. Jafari, K.Gh. Shams, Investigation of Cadmium (II) Ions Biosorption onto Pretreated Dried Activated Sludge, Am. J. Environ. Sci. 5 (2009).

[53] L. Yuan, J. Shen, P. Yan, J. Zhang, Z. Wang, S. Zhao, Z. Chen, Catalytic ozonation of 4-chloronitrobenzene by goethite and Fe2+-modified goethite with low defects: a comparative study, J. Hazard. Mater. 365 (2019) 744–750.

[54] N. Rahemi, M. Haghighi, A.A. Babaluo, M.F. Jafari, P. Estifaee, Synthesis and physicochemical characterizations of Ni/Al2O3–ZrO2 nanocatalyst prepared via impregnation method and treated with non-thermal plasma for CO2 reforming of CH4, J. Ind. Eng. Chem. 19 (2013) 1566–1576.

[55] A. Khataee, P. Gholami, B. Vahid, Heterogeneous sono-Fenton-like process using nanostructured pyrite prepared by Ar glow discharge plasma for treatment of a textile dye, Ultrason. Sonochem. 29 (2016) 213–225.

[56] F. Rashidashmagh, Y. Doekhi-Bennani, M. Tizghadam-Ghazani, J.P. van der Hoek, A. Mashayekh-Salehi, B.S.G.J. Heijman, K. Yaghmaeian, Synthesis and characterization of SnO2 crystalline nanoparticles: A new approach for enhancing the catalytic ozonation of acetaminophen, J. Hazard. Mater. 404 (2021) 124154, https://doi.org/10.1016/j.jhazmat.2020.124154.

[57] A. Khataee, A. Karimi, S. Woo Joo, Sonocatalytic degradation of acid red 17 in the presence of nanosized bio-silica: mechanism and kinetics, Curr. Nanosci. 12 (5) (2016) 621–629.

[58] H. Barndōk, D. Hermosilla Redondo, L. Cortijo Garrido, C. Negro Álvarez, Á. Blanco Suárez, Assessing the effect of inorganic anions on TiO2-photocatalysis and ozone oxidation treatment efficiencies, J. Adv. Oxidation Technol. 15 (2012) 125–132.

[59] A. Khataee, A. Karimi, S. Arefi-Oskoui, R.D.C. Soltani, Y. Hanifehpour, B. Soltani, S. W. Joo, Sonochemical synthesis of Pr-doped ZnO nanoparticles for sonocatalytic degradation of Acid Red 17, Ultrason. Sonochem. 22 (2015) 371–381.

[60] M. Rezakazemi, A.B. Albadarin, G.M. Walker, S.J.I.j.o.b.m. Shirazian, Quantum chemical calculations and molecular modeling for methylene blue removal from water by a lignin-chitosan blend, International Journal of Biological Macromolecules, 120 (2018) 2065-2075.

[61] R. El Haouti, H. Ouachtak, A. El Guerdaoui, A. Amedlous, E. Amaterz, R. Haounati, A.A. Addi, F. Akbal, N. El Alem, M.L. Taha, Cationic dyes adsorption by Na-Montmorillonite Nano Clay: Experimental study combined with a theoretical investigation using DFT-based descriptors and molecular dynamics simulations, J. Mol. Liq. 290 (2019), 111139.

[62] S. Gholami, A.S. Rad, A. Heydarinasab, M. Ardjmand, Adsorption of adenine on the surface of Nickel-decorated graphene; a DFT study, J. Alloys Compounds 686 (2016) 662–668.

[63] M. Sui, L. Sheng, K. Lu, F. Tian, FeOOH catalytic ozonation of oxalic acid and the effect of phosphate binding on its catalytic activity, Appl. Catal. B 96 (2010) 94–100.

[64] O. Oputu, M. Chowdhury, K. Nyamayaro, O. Fatoki, V. Fester, Catalytic activities of ultra-small β-FeOOH nanorods in ozonation of 4-chlorophenol, J. Environ. Sci. 35 (2015) 83–90.

[65] R. Li, H. Du, Z. Fan, J. Pei, Molecular dynamics simulation to investigate the interaction of asphaltene and oxide in aggregate, Adv. Mater. Sci. Eng. 2016 (2016) 3817123.